A&A 578, A49 (2015)
DOI: 10.1051/0004-6361/201525653

Astronomy & Astrophysics

Chemical footprint of star formation feedback in M 82 on scales of ~100 pc[⋆,⋆⋆,⋆⋆⋆]

D. Ginard[1], A. Fuente[1], S. García-Burillo[2], T. Alonso-Albi[2], M. Krips[3], M. Gerin[4], R. Neri[3], P. Pilleri[5,6], A. Usero[2], and S. P. Treviño-Morales[7]

[1] Observatorio Astronómico Nacional (OAN, IGN), Apdo. 112, 28800 Alcalá de Henares, Madrid, Spain
e-mail: `davidginard@gmail.com`
[2] Observatorio Astronómico Nacional (OAN, IGN), Observatorio de Madrid, Alfonso XII, 3, 28014 Madrid, Spain
[3] Institut de Radioastronomie Millimétrique, 300 rue de la Piscine, 38406 Saint Martin d'Hères, France
[4] CNRS UMR 8112, LERMA, Observatoire de Paris and École Normale Supérieure. 24 rue Lhomond, 75231 Paris Cedex 05, France
[5] Université de Toulouse, UPS-OMP, IRAP, 31400 Toulouse, France
[6] CNRS, IRAP, 9 Av. colonel Roche, BP 44346, 31028 Toulouse Cedex 4, France
[7] Instituto de Radioastronomía Milimétrica (IRAM-Spain), Ave. Divina Pastora, 7, 18012 Granada, Spain

Received 13 January 2015 / Accepted 17 February 2015

ABSTRACT

Context. M 82 is one of the nearest and brightest starburst galaxies. It has been extensively studied in the past decade and by now is considered the prototypical extragalactic photon-dominated region (PDR) and a reference for studying star formation feedback.
Aims. Our aim is to characterize the molecular chemistry in M 82 at spatial scales of giant molecular clouds (GMCs), ~100 pc, to investigate the feedback effects of the star formation activity.
Methods. We present interferometric observations of the CN 1 → 0 (113.491 GHz), N_2H^+ 1 → 0 (93.173 GHz), H(41)α (92.034 GHz), CH_3CN (91.987 GHz), CS 3 → 2 (146.969 GHz), c-C_3H_2 $3_{1,2} \rightarrow 2_{2,1}$ (145.089 GHz), H_2CO $2_{0,2} \rightarrow 1_{0,1}$ (145.603 GHz), and HC_3N 16 → 15 (145.601 GHz) lines carried out with the IRAM Plateau de Bure Interferometer (PdBI). PDR chemical modeling was used to interpret these observations.
Results. Our results show that the abundances of N_2H^+, CS and $H^{13}CO^+$ remain quite constant across the galaxy, confirming that these species are excellent tracers of the dense molecular gas. In contrast, the abundance of CN increases by a factor of ~3 in the inner $x2$ bar orbits. The [CN]/[N_2H^+] ratio is well correlated with the H(41)α emission at all spatial scales down to ~100 pc. Chemical modeling shows that the variations in the [CN]/[N_2H^+] ratio can be explained as the consequence of differences in the local intestellar UV field and in the average cloud sizes within the nucleus of the galaxy.
Conclusions. Our high spatial resolution imaging of the starburst galaxy M 82 shows that the star formation activity has a strong impact on the chemistry of the molecular gas. In particular, the entire nucleus behaves as a giant PDR whose chemistry is determined by the local UV flux. The detection of N_2H^+ shows the existence of a population of clouds with $A_v > 20$ mag all across the galaxy plane. These clouds constitute the molecular gas reservoir for the formation of new stars and, although it is distributed throughout the nucleus, the highest concentration occurs in the outer $x1$ bar orbits ($R \sim 280$ pc).

Key words. galaxies: individual: M82 – galaxies: ISM – galaxies: starburst – ISM: abundances – ISM: molecules – astrochemistry

1. Introduction

M 82 is one of the nearest and brightest starburst galaxies. Located at a distance of 3.9 Mpc, and with a luminosity of 3.7×10^{10} $L_\odot$, it has been the subject of continuum and line observations at all wavelengths from X-rays to the radio domains. Several molecular line studies indicate that the strong UV field has heavily influenced the physical conditions, kinematics, and chemistry of the interstellar gas (Mao et al. 2000; Weiss et al. 2001a,b; García-Burillo et al. 2001, 2002; Fuente et al. 2005, 2006, 2008; Aladro et al. 2011). In fact, M 82 has become the prototypical extragalactic photon-dominated region (PDR) and a reference for studying and interpreting star formation feedback in extreme starbursts near and far.

The stellar bar in M 82 has been invoked as a mechanism to fuel the star formation activity in the inner $r \sim 30''$ (500 pc) disk of the galaxy. The stellar bar, studied in detail by Greve et al. (2002), could have formed during the encounter of M 81 and M 82. The orbits sustaining the bar potential, denoted as x_1 orbits, are oriented parallel to the bar major axis and extend out to $r \sim 30''$ (500 pc) in the disk. The M 82 stellar bar seems to have room for $x2$ orbits, which are oriented parallel to the bar minor axis, in the inner $r \sim 5''$ (~90 pc). Evidence supporting the existence of $x2$ orbits in M 82 is derived from the position-velocity diagrams obtained in several tracers of the interstellar medium (ISM), including CO, HI, and [NeII] emission line data (Shen & Lo 1995; Neininger et al. 1998; Wills et al. 2000; Achtermann & Lacy 1995). Coupled stellar population synthesis and photoionization models reveal two major episodes of star formation over the past 10 Myr (Förster-Schreiber et al. 2003). The first episode

---

[⋆] Based on observations carried out with the IRAM Plateau de Bure Interferometer. IRAM is supported by INSU/CNRS (France), MPG (Germany), and IGN (Spain).

[⋆⋆] Appendix A is available in electronic form at http://www.aanda.org

[⋆⋆⋆] FITS files of the reduced data cubes are only available at the CDS via anonymous ftp to `cdsarc.u-strasbg.fr` (`130.79.128.5`) or via `http://cdsarc.u-strasbg.fr/viz-bin/qcat?J/A+A/578/A49`

(∼10 Myr) took place throughout the central regions of M 82 and was particularly intense at the nucleus, while the second episode (∼5 Myr) occurred predominantly in a circumnuclear ring at a radius of ∼90 pc and along the stellar bar. This inside-outside scenario can be understood as resulting from the gravitational interaction between M 82 and its neighbor M 81, and subsequent bar-driven evolution. Each episode only lasted for a few million years, suggesting strong negative feedback effects from the starburst activity.

X-rays and optical observations have shown the existence of a biconical outflow of hot gas exiting the plane in the nucleus of M 82 (Bregman et al. 1995; Shopbell et al. 1998). It is widely accepted that the driving mechanism of the outflow phenomenon in starbursts is linked to the creation of expanding shells of hot gas by supernovae. These hot bubbles blow out into the halo, entraining surrounding cold gas and dust at several hundreds of kilometers per second. Interferometric observations showed that, contrary to most species, the SiO emission does not trace the molecular gas in the galaxy disk. The detection of a ∼500 pc molecular gas chimney and a supershell in SiO indicates the occurrence of large-scale shocks in the disk-halo interface (García-Burillo et al. 2001). Out-of-plane molecular emission has also been detected in CO, HCN, and HCO^+ (Weiss et al. 2001b; Salas et al. 2014). Recent observations of the HCN 1 → 0 and HCO^+1 → 0 lines by Salas et al. (2014) showed that >2% of the total dense molecular gas is in the outflow formed by the gas expelled by the central starburst.

M 82 is one of the finest examples of how chemistry can help to fully understand the ISM of an external galaxy. Our early HCO interferometric map using the Plateau de Bure Interferometer (PdBI) showed that the M 82 nucleus is a giant PDR of ∼650 pc size. Furthermore, the comparison between the HCO and $H^{13}CO^+$ images suggested that the PDR chemistry is propagating across the M 82 nucleus. Our subsequent 30 m and PdBI chemical studies provided further support for the existence of giant PDRs in the galaxy disk (García-Burillo et al. 2002; Fuente et al. 2005, 2006, 2008). In particular, the detection of the reactive ion CO^+ using the 30 m telescope is remarkable (Fuente et al. 2006), which is the first time this is detected in an external galaxy, as well as the interferometric image of the HOC^+1 → 0 line (Fuente et al. 2008), which is the first ever observed. Chemical modeling using the Meudon PDR code showed that most of the observations (CO^+, HOC^+, HCO^+, CN, HCN, and H_3O^+) are well explained assuming that about 87% of the mass of the molecular gas is forming small (∼0.02 pc) clouds with a total thickness of ∼5 mag. In these small clouds all the molecular gas is exposed to an intense UV field, and the entire cloud is a PDR. Additional star formation is not expected in this PDR component. A small mass fraction (∼13%) must, however, be located in shielded regions to account for the measured [CN]/[HCN] abundance ratio. We estimated that these clouds could have high column densities, with a total visual extinction of >50 mag. The existence of this shielded component is also necessary to explain the detection of some species such as NH_3 and CH_3OH (Weiss et al. 2001a; Martín et al. 2006; Aladro et al. 2011).

However, this chemical study was based on single-dish 30 m observations toward one position (position E in the nomenclature of Fuente et al. 2008) and cannot be extrapolated to the entire galaxy. In addition, all the observed molecules were PDR tracers, which are inadequate for tracing the shielded gas. In this paper, we present high spatial resolution (∼100 pc) observations of a set of molecular lines carried out with the PdBI. This set of molecules includes PDR tracers such as CN and c-C_3H_2, but also well-known tracers of cold and dense gas such as N_2H^+, CS and $C^{18}O$. We combine the information from all these molecules to gain insights into the spatial distribution, physical conditions, and chemistry of the molecular gas reservoir in the M 82 starburst.

2. Observations and data reduction

The interferometric observations of the CN 1 → 0 (113.491 GHz), N_2H^+ 1 → 0 (93.173 GHz), CS 3 → 2 (146.969 GHz), c-C_3H_2 $3_{1,2}$ → $2_{2,1}$ (145.089 GHz), H_2CO $2_{0,2}$ → $1_{0,1}$ (145.603 GHz), and HC_3N 16 → 15 (145.601 GHz) lines were carried out with the IRAM PdBI as part of two different projects. The CN 1 → 0 line was imaged in May and December, 2005, with the antennas arranged in C and D configurations, providing an almost circular beam of 2.46″ × 2.27″ PA 170°. The primary beam of the PdBI at this frequency is ∼44″, enough to cover the whole galactic plane at 3 mm, and only one field was observed. During the observations we adjusted the spectral correlator to give a contiguous bandwidth of 1 GHz with a frequency resolution of 2.5 MHz. The continuum maps were generated using the channels free of line emission. Then we subtracted the continuum emission to produce the spectroscopic maps. The maps were corrected for primary beam attenuation (primary beam = 44″ at 113.5 GHz).

In the second project we imaged the N_2H^+ 1 → 0 (93.173 MHz), CS 3 → 2 (146.969 MHz), c-C_3H_2 $3_{1,2}$ → $2_{2,1}$ (145.089 MHz), H_2CO $2_{0,2}$ → $1_{0,1}$ (145.603 MHz), and HC_3N 16 → 15 (145.601 MHz) lines. These observations were carried out in December, 2010 and May, 2011, with the antennas arranged in the C configuration. During the 3 mm observations, the narrow-band correlators were placed to cover the N_2H^+ 1 → 0 line with a frequency resolution of 20 kHz. We used the wide-band correlator WideX to cover a bandwidth of 3.6 GHz in dual polarization with a channel spacing of about 1.95 MHz. This allowed us to observe the H(41)α recombination line at 92.034 GHz and the CH_3CN $5_k \rightarrow 4_k$ $k = 0, 1, 2, 3$ at ∼91.987 GHz simultanously with the N_2H^+ 1 → 0 line (see Fig. 1). Only one field was observed, and the maps were corrected for primary beam attenuation (primary beam = 54″ at 92.5 GHz). The synthesized beam was almost circular with $HPBW \sim 3.56'' \times 2.74''$ PA 94°. Because of the slightly better sensitivity, we used the WideX cube for our analysis.

At 2 mm, we observed two fields at (+7″, +2.5″) and (−7″, −2.5″). The CS 3 → 2 line was covered with the narrow band correlators, providing a frequency resolution of 160 kHz. The wide-band correlator WideX was used to cover a bandwidth of 3.6 GHz in dual polarization with a channel spacing of about 1.95 MHz. This allowed us to observe the H(35)α and the c-C_3H_2 $3_{1,2}$ → $2_{2,1}$, CH_3OH 3 → 2, H_2CO $2_{0,2}$ → $1_{0,1}$ and HC_3N 16 → 15 lines in the same setting. In Fig. 1 we present the observed spectrum toward the position (+14″, +5″). Unfortunately, the c-C_3H_2 line is blended with several CH_3OH 3 → 2 lines and cannot be separated (see Fig. 1). The H_2CO $2_{0,2}$ → $1_{0,1}$ (145.603 MHz) and HC_3N 16 → 15 (145.601 MHz) lines are partially blended and cannot be imaged separately, but can be separated in the outer part of the galaxy where the line widths are narrower. We generated continuum maps using the channels free of line emission to subtract the continuum from the spectral images. The HPBW of the synthesized beam is ∼2.3″ × 1.88″ PA 75°.

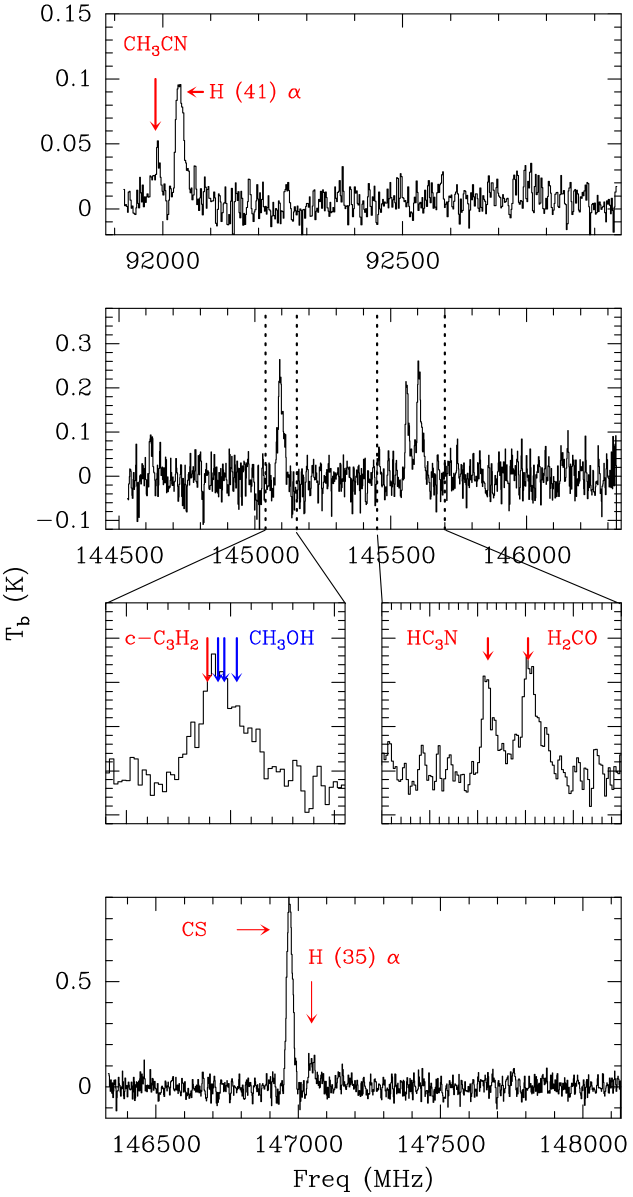

Fig. 1. Interferometric spectra toward E1 [offset (+14″, +5″)] in temperature units (K). The velocity has been set to $v_{\rm lsr}$ = 330 km s^{-1}, based on the $C^{18}O$ data. Vertical lines indicate the following frequencies: 91987 (CH_3CN $5_0 \rightarrow 4_0$), 92034 (H(41)α), 145561 (HC_3N 16 → 15), 145603 (H_2CO $2_{0,1} \rightarrow 1_{0,1}$), 145089 (c-$C_3H_2$ $3_{1,2} \rightarrow 2_{2,1}$), 145094 (E-$CH_3OH$ $3_{0,0} \rightarrow 2_{0,0}$), 145097 (E-$CH_3OH$ $3_{-1,0} \rightarrow 2_{-1,0}$), 145103 (A-$CH_3OH$ $3_{0,0} \rightarrow 2_{0,0}$), 146969 (CS 3 → 2), and 147047 (H(35)α) MHz.

Data analysis and image processing were made using the GILDAS package software[1] and JPARSEC[2].

All the maps are centered at RA = 09:55:51.9, Dec = +69:40:47.10 (J2000), that is, the 2.2 μm peak as determined by Joy et al. (1987). This is also the central position used in previous interferometric studies (Weiss et al. 2001b; García-Burillo et al. 2001, 2002; Fuente et al. 2008). Lester et al. (1990) established the 2 μm peak at RA = 09:55:52.4, Dec = +69:40:46.00 (J2000), i.e. +2.7″ E 1.3″ S from our center position. The M 82 galactic plane is viewed almost edge-on ($i \sim 80°$, Greve 2011). In order to guide the discussion, we have defined four positions E1, E2, W2, and W1 [(+14″, +5″), (+5″, +2″), (−5″, −2″) and (−14″, −5″), respectively] that are aligned with the center at an angle of 68°. Within the errors, this is the position angle of the galactic plane. The intense continuum source SN 41.9+58 is located (−1.25″, −1.1″) from our position W2 (Kronberg et al. 1981; Weiss et al. 1999). Position E1 coincides with position E in Fuente et al. (2008). The stellar bar is inclined ~4° relative to the galactic plane, with the western side above the adopted major axis of the disk. This explains the tilted appearance in the molecular emission (see Figs. 2 and 3).

In addition to these new observations, we used previous interferometric data published by García-Burillo et al. (2001), Fuente et al. (2008), and Weiss et al. (2001b). In Table 1, we briefly describe the observations and their more relevant observational parameters.

3. Results

Figure 1 shows the wide-band spectra toward E1. The velocity-integrated intensity maps for all the lines detected are shown in Figs. 2 and 3. The maps of the H_2CO $2_{0,2} \rightarrow 1_{0,1}$ (145.603 MHz) and HC_3N 16 → 15 (145.601 MHz) are not shown because the lines cannot be deblended in the inner region. In Fig. 4, we show the position-velocity (p-v) diagrams along the galactic plane (straight line across E1, E2, W2, and W1) of the H_2CO $2_{0,2} \rightarrow 1_{0,1}$, HC_3N 16 → 15, CH_3CN $5_k \rightarrow 4_k$, and H(41)α lines. The CH_3CN $5_k \rightarrow 4_k$ is only detected toward the outer part of the galaxy and, at 3σ level, around W2. We subtracted the CH_3CN $5_k \rightarrow 4_k$ line from the data cube to create the H(41)α map shown in Fig. 2. In Fig. 3, we show the c-C_3H_2 map, although we are aware that the line is contaminated with CH_3OH emission. We discuss this problem in Sect. 4.

3.1. Galactic plane

The emissions of all the species studied in this paper are concentrated in the galactic plane. However, there are some differences in their spatial distributions that we discuss below.

In Fig. 2 we show the integrated intensity maps of the lines that present intense emission toward the inner positions, E2 and W2. E2 and W2 are related with the ring of ionized gas that is associated with the most recent starburst (~5 Myr) (Förster-Schreiber et al. 2011). This ring is asymmetric, with the western part more intense than the eastern one. The continuum emission at 3 mm and the ionized line [NeII] are highest toward W2 (see Fuente et al. 2008 and Fig. 2). As expected, the emission of H(41)α follows the same spatial distribution. The emissions of the molecular lines are, however, more intense in the outer part of the galaxy close to positions E1 and W1, with the only exception of CN, which presents its emission peak toward the inner ring, following the spatial distribution of the ionized lines. CN is known to present higher abundances in regions with enhanced UV fields (Fuente et al. 1993, 1995; Bachiller et al. 1997; Boger & Sternberg 2005). Its peculiar spatial distribution suggests that the UV radiation from the recently formed stars has a strong impact on the molecular gas chemistry in the inner ring.

The emission of most molecular lines, $H^{13}CO^+$ 1 → 0, HOC^+ 1 → 0, $C^{18}O$ 1 → 0, HCO 1 → 0, C_3H_2 $3_{1,2} \rightarrow 2_{2,1}$, and CS 3 → 2 is, however, more intense toward the outer positions, E1 and W1 (see Fig. 3). Although all these molecules are brighter in the outer part of the galaxy, the exact positions of their emission peaks differ, especially in the western part. The C_3H_2 $3_{1,2} \rightarrow 2_{2,1}$, CS 3 → 2, $H^{13}CO^+$ 1 → 0, and HOC^+ 1 → 0 peaks

---

[1] http://www.iram.fr/IRAMFR/GILDAS/

[2] http://conga.oan.es/~alonso/doku.php?id=jparsec

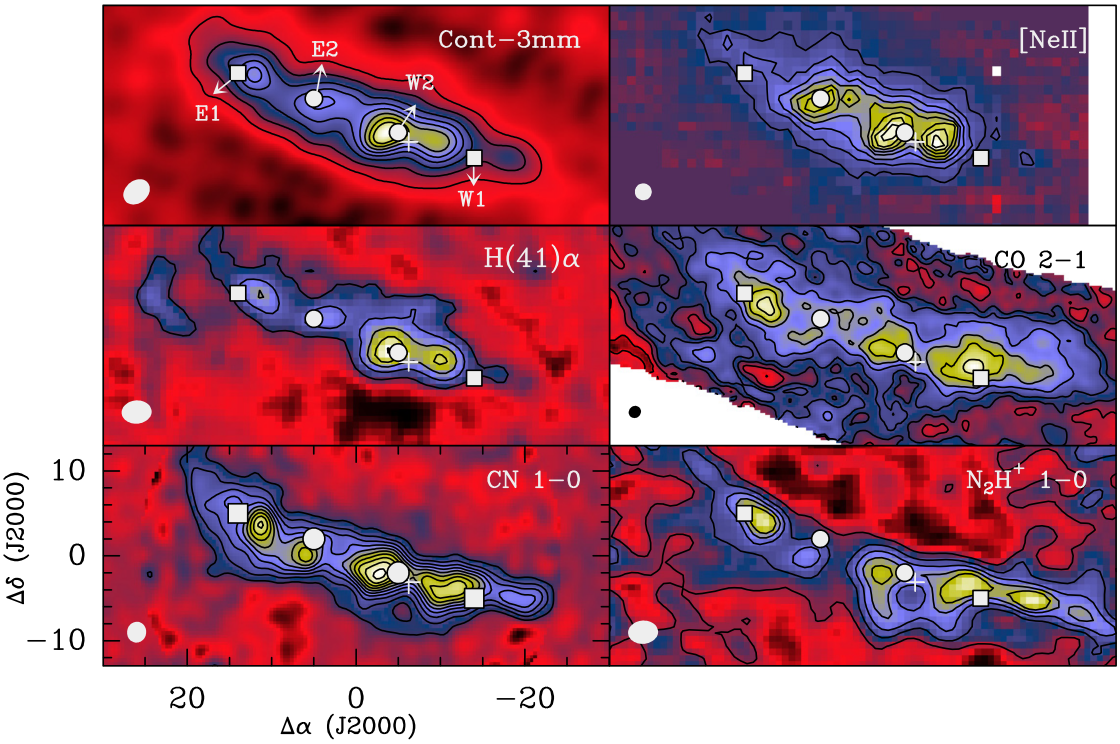

Fig. 2. Map of the continuum emission at 3 mm (Fuente et al. 2008) and line-integrated intensity maps of the 12.8 μm line of [NeII] (Achtermann & Lacy 1995), H(41)α, CO 2 → 1, CN 1 → 0, and N_2H^+ 1 → 0 lines. The beam is drawn in the lower left corner of the panels, and positions E1, E2, W2, and W1 are indicated by filled polygons. The position of SN 41.9+58 is marked with a white cross. First contour is at $3 \times \sigma$ level. Contour levels are 1.7 mJy/beam, 5 mJy/beam to 35 mJy/beam in steps of 5 mJy/beam (cont – 3 mm); 0.13 Jy/beam to 1.04 Jy/beam in steps of 0.13 Jy/beam ([NeII]); 4 to 28 in steps of 4 $\mathrm{K} \times \mathrm{km\,s^{-1}}$ (H(41) α); 200, 400, 600, 800, 1200, 1600, 2000, 2400 $\mathrm{K} \times \mathrm{km\,s^{-1}}$ (CO); 15.8 to 252.8 in steps of 15.8 $\mathrm{K} \times \mathrm{km\,s^{-1}}$ (CN); 2.5, 5.0, 7.5, 10.0, 12.5 $\mathrm{K} \times \mathrm{km\,s^{-1}}$ (N_2H^+). Color scale is adjusted to the lowest and highest values in each panel.

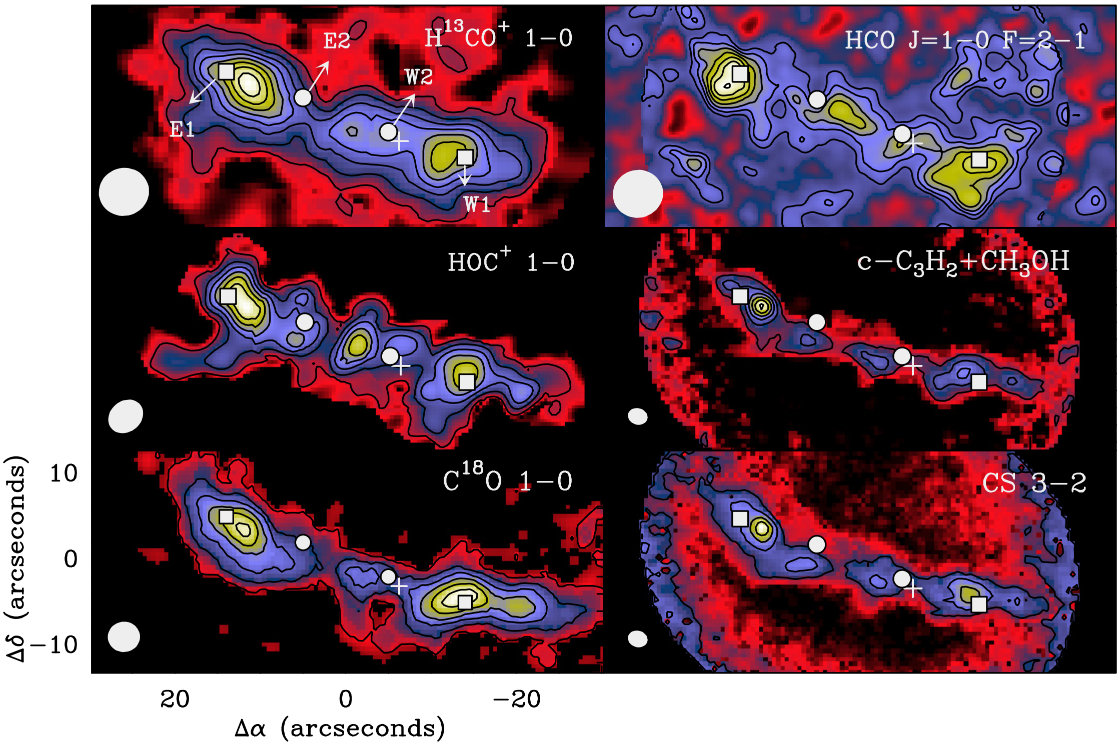

Fig. 3. Same as Fig. 2 for the $H^{13}CO^+$ 1 → 0, HCO 1 → 0 F = 2 → 1, HOC^+ 1 → 0, C_3H_2 $3_{1,2} \rightarrow 2_{2,1}$, $C^{18}O$ 1 → 0 and CS 3 → 2 lines. Contour levels are 0.6 to 4.6 in steps of 0.6 $\mathrm{K} \times \mathrm{km\,s^{-1}}$ ($H^{13}CO^+$); 0.7 to 1.9 in steps of 0.2 $\mathrm{K} \times \mathrm{km\,s^{-1}}$ (HCO); 0.28, 0.70, 1.12,1.54, 1.96, 2.38 $\mathrm{K} \times \mathrm{km\,s^{-1}}$ (HOC^+); 6.4 to 44.8 in steps of 6.4 $\mathrm{K} \times \mathrm{km\,s^{-1}}$ (C_3H_2); 2, 8, 14, 20, 26, 32 $\mathrm{K} \times \mathrm{km\,s^{-1}}$ ($C^{18}O$); 30 to 150 in steps of 30 $\mathrm{K} \times \mathrm{km\,s^{-1}}$ (CS).

Table 1. Observations.

Line		Freq. (GHz)	Beam (″)	Fields	T_b/Flux K/(Jy/beam)	Date or reference[1]
$C^{18}O$	$1 \rightarrow 0$	109.782	3.8″ × 3.5″ PA −4°	(0″, 0″)	7.6	W01 (Zero-spacing)
CO	$2 \rightarrow 1$	230.538	1.5″ × 1.4″ PA 0°	(−30″, −8″), (−20″, −6″) (−10″, −4″), (10″, 4″) (20″, 8″), (30″, 10″)	11	W01 (Zero-spacing)
CN	$1 \rightarrow 0$	113.491	2.5″ × 2.3″ PA 170°	(0″, 0″)	17	May–Dec. 2005
$H^{13}CO^+$	$1 \rightarrow 0$	86.754	5.9″ × 5.6″ PA 105°	(0″, 0″)	5	G01
HCO	$1 \rightarrow 0$	86.670	5.9″ × 5.6″ PA 105°	(0″, 0″)	5	G01
HOC^+	$1 \rightarrow 0$	89.487	4.4″ × 3.6″ PA 128°	(0″, 0″)	9	F08
N_2H^+	$1 \rightarrow 0$	93.173	3.6″ × 2.7″ PA 94°	(0″, 0″)	14	Dec. 2010–May 2011
H	(41) α	92.034	3.5″ × 2.8″ PA 94°	(0″, 0″)	15	Dec. 2010–May 2011
CH_3CN	$5_3 \rightarrow 4_0$	91.971	3.5″ × 2.8″ PA 94°	(0″, 0″)	15	Dec. 2010–May 2011
	$5_2 \rightarrow 4_2$	91.980	3.5″ × 2.8″ PA 94°	(0″, 0″)	15	Dec. 2010–May 2011
	$5_1 \rightarrow 4_1$	91.985	3.5″ × 2.8″ PA 94°	(0″, 0″)	15	Dec. 2010–May 2011
	$5_0 \rightarrow 4_0$	91.987	3.5″ × 2.8″ PA 94°	(0″, 0″)	15	Dec. 2010–May 2011
H	(35) α	147.047	2.3″ × 1.9″ PA 75°	(+7″, +2.5″), (−7″, −2.5″)	13	Dec. 2010–May 2011
CS	$3 \rightarrow 2$	146.969	2.3″ × 1.9″ PA 75°	(+7″, +2.5″), (−7″, −2.5″)	12	Dec. 2010–May 2011
$c\text{-}C_3H_2$	$3_{1,2} \rightarrow 2_{2,1}$	145.089	2.3″ × 1.9″ PA 75°	(+7″, +2.5″), (−7″, −2.5″)	12	Dec. 2010–May 2011
$A\text{-}CH_3OH$	$3_{0,0} \rightarrow 2_{0,0}$	145.103	2.3″ × 1.9″ PA 75°	(+7″, +2.5″), (−7″, −2.5″)	12	Dec. 2010–May 2011
$E\text{-}CH_3OH$	$3_{0,0} \rightarrow 2_{0,0}$	145.094	2.3″ × 1.9″ PA 75°	(+7″, +2.5″), (−7″, −2.5″)	12	Dec. 2010–May 2011
	$3_{-1,0} \rightarrow 2_{-1,0}$	145.097	2.3″ × 1.9″ PA 75°	(+7″, +2.5″), (−7″, −2.5″)	12	Dec. 2010–May 2011
H_2CO	$2_{0,2} \rightarrow 1_{0,1}$	145.603	2.3″ × 1.9″ PA 75°	(+7″, +2.5″), (−7″, −2.5″)	12	Dec. 2010–May 2011
HC_3N	$16 \rightarrow 15$	145.561	2.3″ × 1.9″ PA 75°	(+7″, +2.5″), (−7″, −2.5″)	12	Dec. 2010–May 2011

References. (1) W01: Weiss et al. (2001b) ; G01: García-Burillo et al. (2001); F08: Fuente et al. (2008).

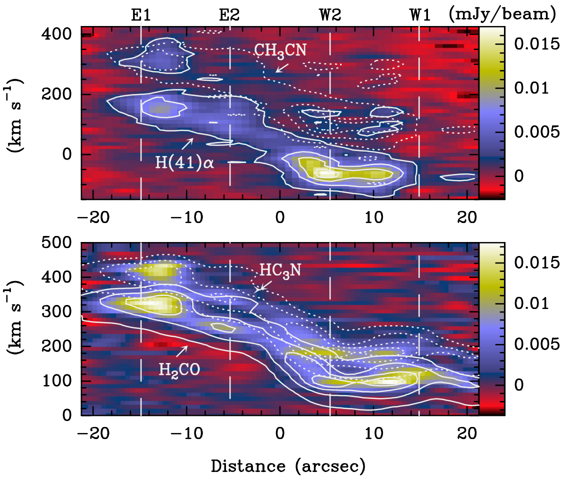

Fig. 4. *Top*: in color scale, the position-velocity (*p-v*) diagram along the galactic plane (crossing E1, E2, W2, and W1) of H(41)α. Solid contours are the 2.1 mJy/beam to 16.6 mJy/beam by 4.2 mJy/beam. As dashed lines, we plot the same contours, but centered at the frequency of CH_3CN $5_0 \rightarrow 4_0$ line (91.987 GHz). *Bottom*: in color scale, the *p-v* diagram of the H_2CO $2_{0,1} \rightarrow 1_{0,1}$ line. For comparison, we have drawn in solid contours the levels of the CN $1 \rightarrow 0$ line: 10.0 mJy/beam to 86.6 mJy/beam by 20.0 mJy/beam. As dashed lines, the same contours are plotted at the frequency of the HC_3N $16 \rightarrow 15$ line. Note that the H_2CO $2_{0,1} \rightarrow 1_{0,1}$ and HC_3N $16 \rightarrow 15$ lines are heavily blended in the inner region.

are located 2″–4″ closer to the dynamical center of the galaxy than HCO $1 \rightarrow 0$. The intense peak of the $c\text{-}C_3H_2$ line toward E1 is very likely due to the CH_3OH contamination (see Sect. 4).

In Fig. 5 we show the *p-v* diagrams of the CN $1 \rightarrow 0$/N_2H^+ $1 \rightarrow 0$, CN $1 \rightarrow 0$/CS $3 \rightarrow 2$ and the CS $3 \rightarrow 2$/N_2H^+ $1 \rightarrow 0$ line ratios along the plane defined by positions E1, E2, W1, and W2. To perform these diagrams, we degraded the spatial and spectral resolutions of the three line intensity cubes to common values of 3.8″ and 12 km s^{-1}. We adopted $3 \times \sigma$ as the threshold for line detection. There is a clear gradient in the CN $1 \rightarrow 0$/N_2H^+ $1 \rightarrow 0$ line ratio along the galaxy plane, which is a factor of ~3 higher in the inner region than in E1. For comparison, we show the *p-v* diagram of the $C^{18}O$ $1 \rightarrow 0$ /H(41)α line ratio that can be considered as an observational tracer of the gas illumination. There are two regions where the CN $1 \rightarrow 0$/N_2H^+ $1 \rightarrow 0$ takes the peak value of ~15: (i) W2, which is the peak in the H(41)α line emission and the region with the highest concentration of HII regions; and (ii) E2, the emission of the H(41)α line is lower than in W2, but the molecular gas column density is also lower, especially in the ~326 km s^{-1} component that is not detected in N_2H^+ (see Sect. 3.2); as a consequence, the molecular gas is very likely immersed in a high UV field (see Fig. 5A). The CN $1 \rightarrow 0$/CS $3 \rightarrow 2$ line ratio has a ratio ~1−2 along the cut and increases to ~5 only in the two enhanced UV field regions described above (see Fig. 5C). The variations of these two molecular line ratios are not haphazardly but seem to be related with the distribution of the ionized gas, which suggests that UV photons are the driving agent of the molecular chemistry. In Fig. 6 we show the log-log correlation diagrams between the CN $1 \rightarrow 0$/N_2H^+ $1 \rightarrow 0$ and CN $1 \rightarrow 0$/CS $3 \rightarrow 2$ line ratios and $C^{18}O$ $1 \rightarrow 0$ /H(41)α. As expected, there is a good (anti-) correlation between these ratios at low extinctions (low values of $C^{18}O$ $1 \rightarrow 0$ /H(41)α). At high extinctions, the dispersion is higher since we can have PDRs (diffuse clouds, the external layers of giant molecular clouds, dense gas around Herbig Ae/Be stars) that do not emit in H(41)α, but also present enhanced CN abundances (see, e.g., Fuente et al. 1993, 1995; Liszt et al. 2001). In contrast, although with a high dispersion, the CS $3 \rightarrow 2$/N_2H^+ $1 \rightarrow 0$ line ratio is ~5 toward all positions.

3.2. Vertical distribution of the molecular emission

M 82 is associated with a kpc-scale outflow with the gas coming toward us in the northern part. Optical and near-infrared

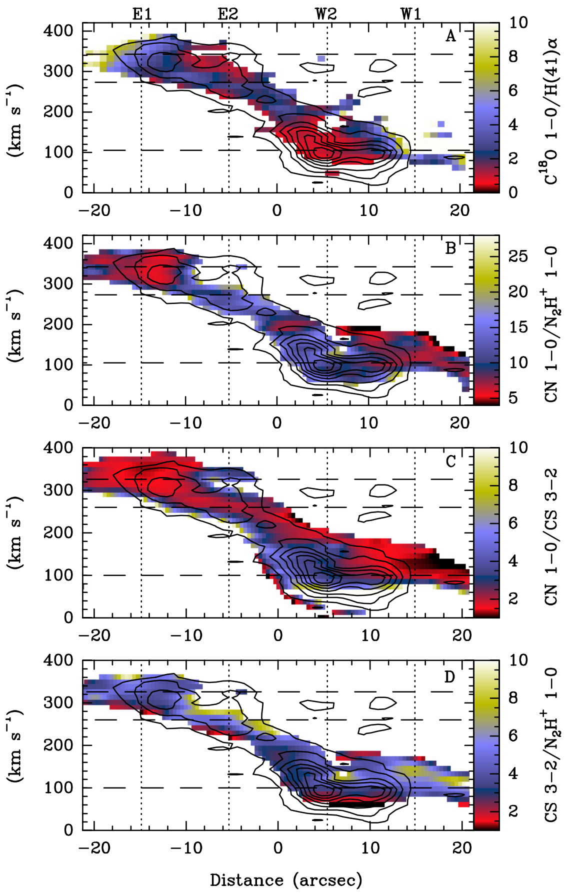

Fig. 5. *p*-*v* diagrams along a cut crossing E1, E2, W2, and W1. Contours correspond to the line intensity of H(41)α (2.1 to 16.6 in steps of 2.1 mJy/beam). Color scale shows the following line intensity ratios (in T_b units): **A)** C^{18}O 1 → 0/H(41)α; **B)** CN 1 → 0/N$_2$H$^+$ 1 → 0; **C)** CN 1 → 0/[CS] 3 → 2; **D)** CS 3 → 2/N$_2$H$^+$ 1 → 0. Horizontal lines correspond to velocities of 100, 270 and 326 km s^{-1}, to facilitate the comparison with Fig. 7. Line ratios have been calculated with the original images degraded to common angular resolution of 3.8″ and a velocity resolution of 12 km s^{-1}. The C^{18}O 1 → 0/H(41)α line ratio can be considered as an observational measurement of the gas illumination by UV photons. Note that the CN/N$_2$H$^+$ and CN/CS line ratios increase in the highest UV irradiated regions, i.e., lowest values of the C^{18}O 1 → 0/H(41)α line ratio.

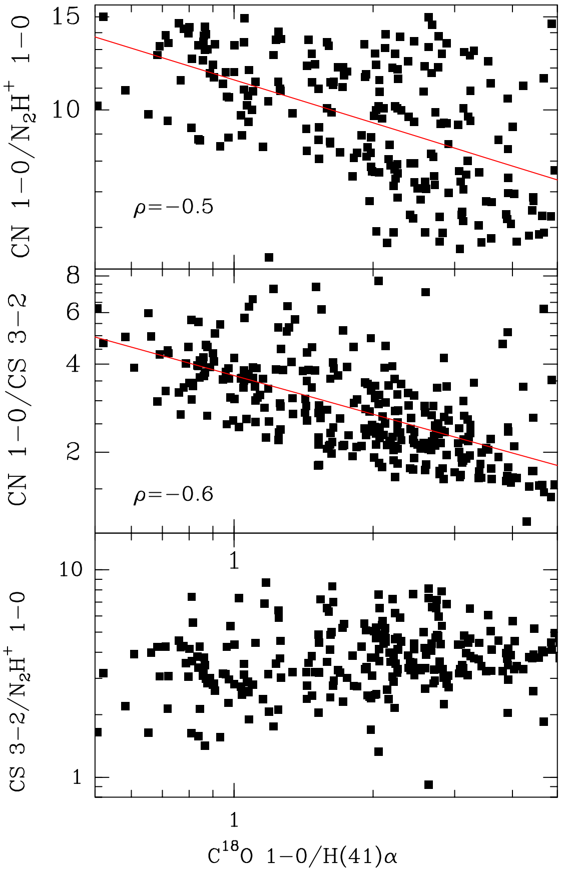

Fig. 6. Correlations between the C^{18}O 1 → 0/H(41)α, CN 1 → 0/N$_2$H$^+$ 1 → 0, and CS 3 → 2/N$_2$H$^+$ 1 → 0 brightness temperature line ratios along the galactic plane shown in Fig. 5. The plots are in logarithmic scale. To obtain a more reliable result that avoids the line borders, we only considered the points within the following range of values: 0.5 and 5 for C^{18}O 1 → 0/H(41)α line; 5 and 15 for CN 1 → 0/N$_2$H$^+$ 1 → 0; 1 and 6 for CN 1 → 0/CS 3 → 2 between 1 and 6. The results of the least-squares fitting and the values of the Pearson correlation coefficients are shown in the *top and middle panels*.

lines look asymmetric, with the most intense half toward the north where the radio continuum chimneys are located (Wills et al. 1999). This asymmetry is also detected in the emission of H(41)α, which proves that it is not a consequence of the dust extinction but to the spatial distribution of the massive star-forming regions located in the northern half of the disk (see Fig. 7). In contrast, the molecular emission extends to ~7.5″ south of the galactic plane, following the molecular supershell around the supernova remnant SN 41.9+58. There are strong differences between the vertical spatial distribution of the different species in the molecular emission.

It is interesting to compare the HCO$^+$ and HOC$^+$ emissions. Fuente et al. (2008) found a clear north-south gradient in the [HCO$^+$]/[HOC$^+$] ratio. This ratio is highest toward the southern part of the supershell associated with SN 41.9+58. The maximum in the HOC$^+$ emission is shifted by ~2.5″ north relative to H^{13}CO$^+$, which means that it is closer to the ionized layer traced by H(41)α. Fuente et al. (2008) interpreted this gradient as a change in the global ionization degree of the molecular clouds.

We used the CN, N$_2$H$^+$, CS, and H(41)α images for an in-depth study of the kinematics and spatial distribution of the molecular gas in the direction perpendicular to the galaxy plane. In Fig. 7 we show the *p*-*v* diagrams in the vertical direction across E2, the dynamic center of the galaxy, and W2. In these diagrams, the velocity axis was re-binned to channels of 12 km s^{-1}.

Toward E2, several velocity components are detected in the H(41)α and molecular lines. All these components are within the range of velocities of the *x*2 bar orbits, ±120 km s^{-1} (Greve 2011). The component at ~260 km s^{-1} is the most intense in molecular emission and is detected in CN, N$_2$H$^+$, and CS. However, the component at ~326 km s^{-1} is well detected in the CN 1 → 0 line, only tentatively detected in CS 3 → 2 ($3 \times \sigma$ level), and remains undetected in the N$_2$H$^+$ 1 → 0 line. This component is associated with a secondary peak in the H(41)α emission. In the right panel, we show the CN 1 → 0/N$_2$H$^+$ 1 → 0 line intensity ratio. It varies between ~10 and ~15 along this cut, with the peaks following the peaks of the H(41)α emission.

Several velocity molecular components are also detected toward W2. In this case, we can also observe a layered structure in the vertical direction with the H(41)α and CN emission being extended toward north, while N$_2$H$^+$ emission is more extended toward the south. Again, there are strong chemical differences between the ~100 km s^{-1} (north) and ~160 km s^{-1} (south)

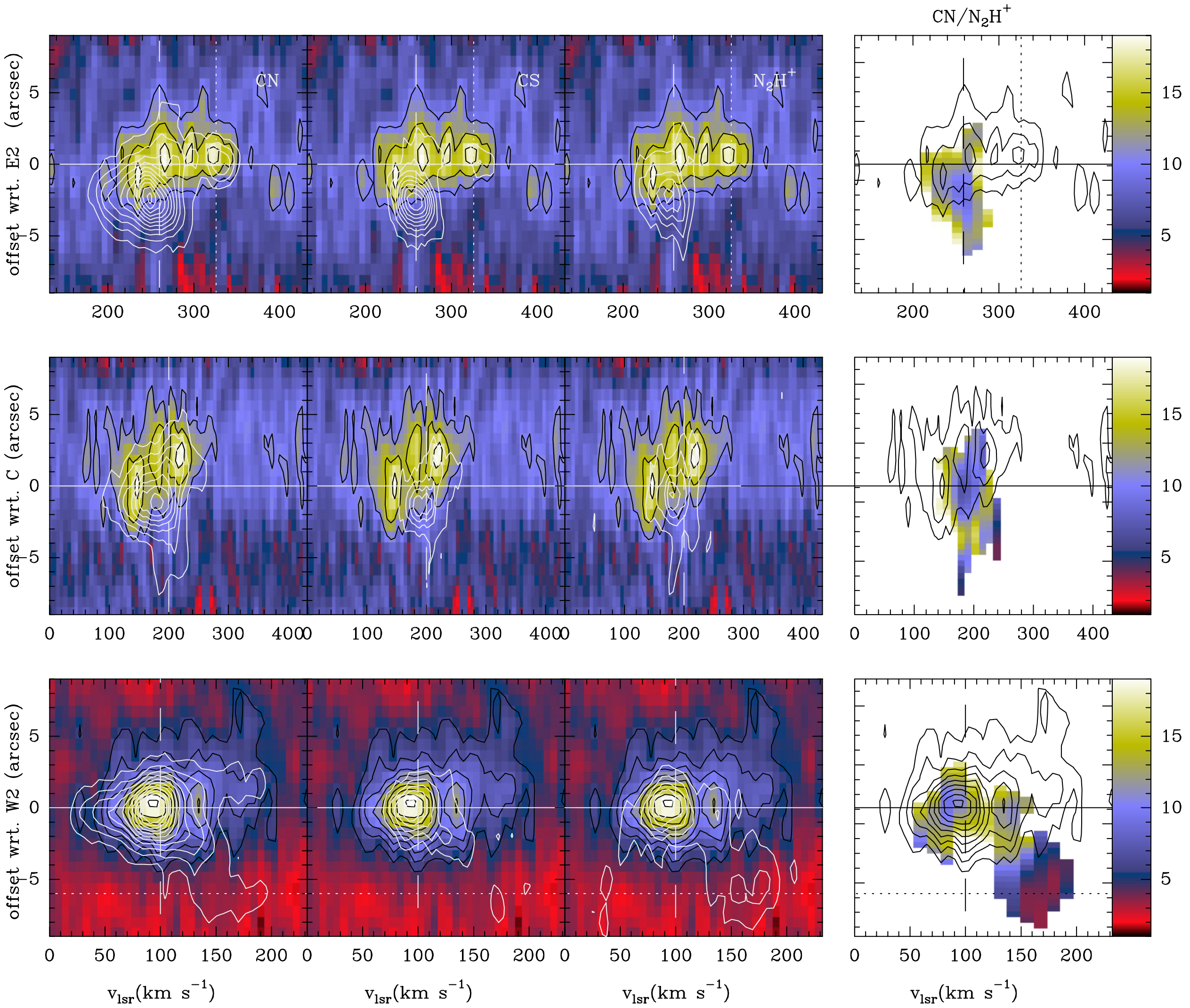

Fig. 7. *p-v* diagrams along cuts perpendicular to the galactic plane at E2 (*top*), the (0, 0) position (*middle*) and W2 (*bottom*). Color scale and black contours correspond to the H(41)α emission. White contours are intensities of the CN 1 → 0, CS 3 → 2 and N_2H^+ 1 → 0 lines. First contours ($3 \times \sigma$) and steps are 10 mJy/beam for CN and CS, 2 mJy/beam for N_2H^+, and H(41)α. The CN 1 → 0/N_2H^+ 1 → 0 line intensity (in T_b units) ratio along these cuts is shown in the *right column*. The images have been degraded to a angular resolution of 3.8″ and a velocity resolution of 12 km s^{-1} to show this line ratio. Vertical lines indicate the position of the velocity components discussed in the text.

components. The northern component is more intense in CN and CS, while the southern component is brighter in the N_2H^+ emission. The CN 1 → 0 /N_2H^+1 → 0 line intensity ratio shows an excellent correlation with the H(41)α emission, with a contrast of a factor of ~5 between the northern and southern components. The lowest values, ~2–3, are found toward the south and are even lower than those observed in the outer part (E1, W1) of the galaxy (see Fig. 5).

For comparison, we also show the *p-v* diagram across the dynamic center of the galaxy. The H(41)α emission is detected shifted toward the north compared with the molecular emission. Similarly to the vertical cut across E2, the CN 1 → 0 /N_2H^+1 → 0 line intensity ratio vary between ~10 and ~15 with the peaks toward the peaks of the H(41)α emission, suggesting that it is a general trend throughout the galactic nucleus.

4. Column densities toward selected positions

4.1. CN, N_2H^+, c-C_3H_2, and CS

The high angular and spectral resolutions provided by our new data, CN 1 → 0, N_2H^+ 1 → 0, H(41)α, CS 3 → 2, and C_3H_2 3 → 2, allow us to carry out a detailed chemical study of the ISM in M 82. The spectral cubes of all these lines were degraded to a common angular resolution of 3.8″ (≈70 pc) and a channel width of 12.8 km s^{-1}, which are typical values for the size and line width of a giant molecular cloud (see, e.g., Murray 2011). From these data, we selected 12 molecular position-velocity peaks (see Fig. 8) to carry out our chemical modeling. The selection criteria were that the knots must be (i) intense and (ii) clearly identified in velocity and position. In addition, the whole set must represent the variety of physical and chemical conditions in the galaxy. The intense and compact emission toward these positions minimizes the uncertainties caused by spatial filtering effects. The selected knots are listed in Table 2 and are indicated in Figs. 8 and A.1–A.3.

GP1 to GP6 are compact molecular peaks in the galactic plane that follow the velocity pattern of the *x*1 and *x*2 bar orbits. These knots have been detected in all molecular lines (see Figs. 8 and A.1–A.3). We added five positions, SS1 to SS5, placed in the supershell associated with SN 41.9+58. Note that SS1 and SS2 are very close to GP4 in the plane of sky and are only distinguishable because of their different velocities. By examining

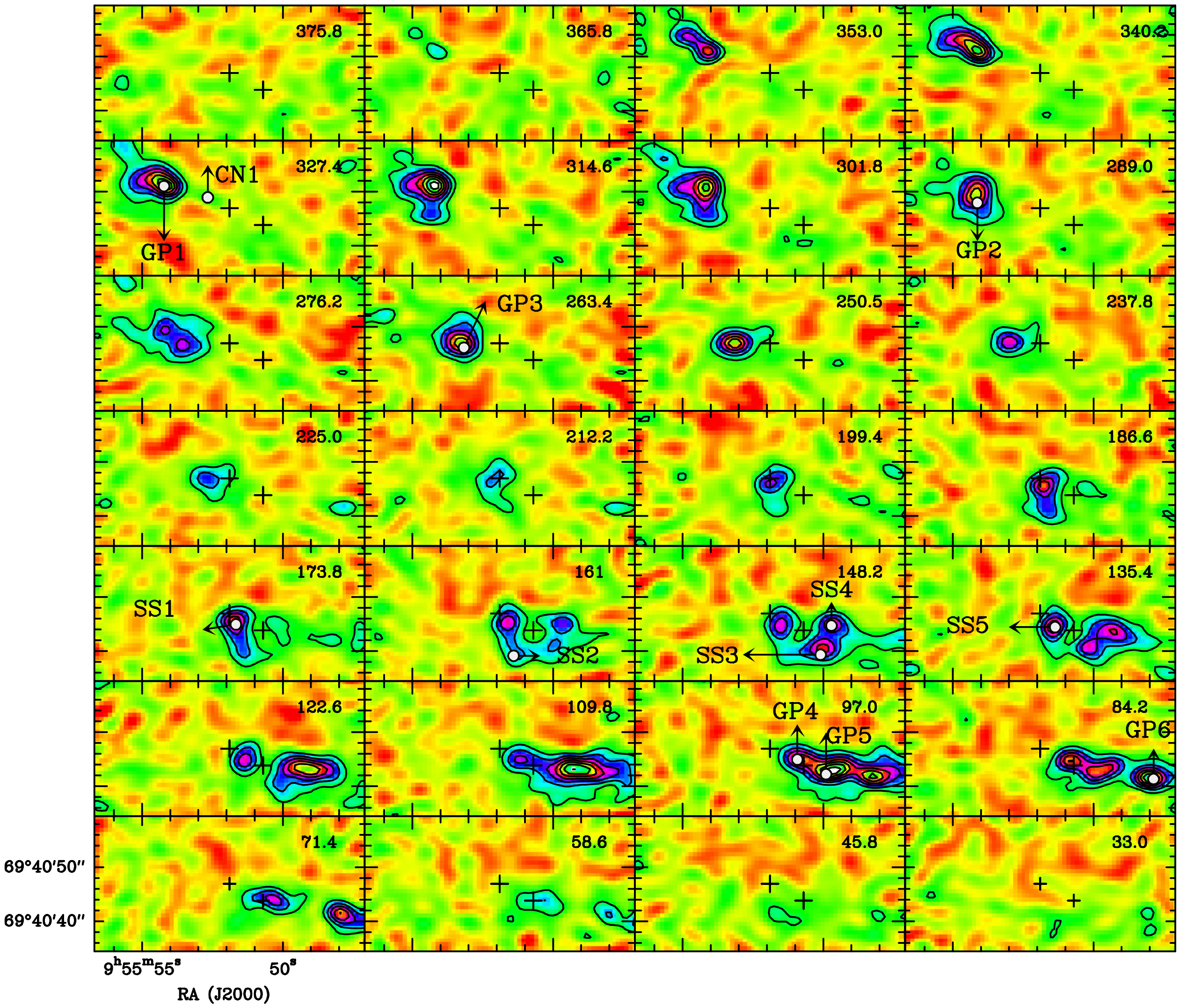

Fig. 8. Spectral maps of the N_2H^+ 1 → 0 line convolved to an angular resolution of 3.8″. To increase the signal-to-noise ratio, the velocity resolution has been degraded to 12.8 km s^{-1}. The number in the upper right corner indicates the central channel velocity. First contour and steps are 0.028 K ($\sim 3 \times \sigma$). Crosses indicate the dynamical center of the galaxy and the position of SN 41.9+58.

Table 2. Selected regions for the chemical model.

Point	Offset (″)	Vel (km s^{-1})	N($C^{18}O$) (×10^{16} cm^{-2})	X(CN) (×10^{-9})	X(N_2H^+) (×10^{-11})	X(o-C_3H_2)[1] (×10^{-10})	X(CS) (×10^{-10})	[CN]/[N_2H^+]	[CS]/[N_2H^+]	[CN]/[CS]
GP1	+12.1 +4.1	327.4	$2.2^{+1.2}_{-1.0}$	$0.9^{+0.8}_{-0.3}$	$3.0^{+1.8}_{-1.3}$	$3.2^{+3.0}_{-1.7}$	$3.0^{+3.9}_{-1.1}$	33^{+17}_{-11}	12^{+8}_{-6}	$3.0^{+0.5}_{-0.5}$
GP2	+11.6 +1.0	289.0	$1.8^{+1.0}_{-0.8}$	$1.0^{+0.8}_{-0.3}$	$2.8^{+1.3}_{-1.4}$	$2.6^{+2.7}_{-1.4}$	$3.2^{+3.6}_{-1.3}$	41^{+22}_{-13}	13^{+10}_{-6}	$3.3^{+0.5}_{-0.5}$
GP3	+6.6 –0.8	263.4	$1.8^{+1.0}_{-0.8}$	$1.4^{+1.0}_{-0.5}$	$3.0^{+1.4}_{-1.6}$	$3.0^{+3.3}_{-1.5}$	$3.8^{+4.3}_{-1.5}$	49^{+23}_{-16}	14^{+10}_{-6}	$3.7^{+0.6}_{-0.7}$
GP4	–5.1 –2.0	97.0	$0.9^{+0.5}_{-0.4}$	$3.0^{+2.1}_{-1.1}$	$4.3^{+2.0}_{-2.1}$	$2.6^{+2.8}_{-1.4}$	$3.5^{+5.2}_{-1.2}$	80^{+34}_{-28}	11^{+8}_{-5}	$7.4^{+1.4}_{-1.5}$
GP5	–10.4 –4.7	97.0	$1.9^{+1.1}_{-0.9}$	$1.4^{+1.0}_{-0.4}$	$3.2^{+1.5}_{-1.6}$	$2.4^{+2.7}_{-1.2}$	$2.6^{+3.6}_{-1.0}$	49^{+23}_{-16}	11^{+7}_{-5}	$4.8^{+0.9}_{-0.9}$
GP6	–21.1 –5.6	84.2	$2.1^{+1.1}_{-1.0}$	$0.8^{+0.6}_{-0.3}$	$3.1^{+1.5}_{-1.5}$	$1.5^{+1.7}_{-0.8}$	$1.8^{+2.5}_{-0.7}$	28^{+13}_{-10}	7^{+6}_{-3}	$3.8^{+0.6}_{-0.6}$
SS1	–1.2 –2.0	173.8	$1.0^{+0.5}_{-0.5}$	$2.0^{+1.6}_{-0.7}$	$4.8^{+2.3}_{-2.4}$	$3.1^{+3.5}_{-1.2}$	$2.9^{+4.3}_{-1.0}$	47^{+23}_{-16}	8^{+5}_{-5}	$6.2^{+1.0}_{-1.2}$
SS2	–2.6 –7.8	161.0	$0.6^{+0.3}_{-0.3}$	$0.9^{+0.8}_{-0.3}$	$3.8^{+1.9}_{-1.8}$	$1.4^{+1.6}_{-0.7}$	$1.1^{+1.8}_{-0.7}$	28^{+13}_{-10}	4^{+3}_{-2}	$7.5^{+1.4}_{-1.4}$
SS3	–9.4 –7.6	148.2	$1.4^{+0.7}_{-0.7}$	$0.5^{+0.4}_{-0.2}$	$2.7^{+1.4}_{-1.3}$	$1.4^{+1.7}_{-0.7}$	$1.0^{+1.5}_{-0.4}$	19^{+11}_{-7}	5^{+4}_{-3}	$4.2^{+0.6}_{-0.8}$
SS4	–13.3 –2.9	148.2	$1.5^{+0.7}_{-0.7}$	$0.9^{+0.7}_{-0.3}$	$2.7^{+1.3}_{-1.3}$	$2.2^{+2.1}_{-1.0}$	$2.4^{+2.6}_{-1.1}$	38^{+19}_{-13}	5^{+4}_{-3}	$4.0^{+0.7}_{-0.7}$
SS5	–2.8 –2.5	135.4	$1.1^{+0.5}_{-0.5}$	$2.4^{+1.9}_{-0.8}$	$4.2^{+2.0}_{-2.0}$	$2.6^{+2.9}_{-1.3}$	$2.6^{+3.9}_{-0.9}$	66^{+29}_{-23}	10^{+7}_{-5}	$8.3^{+1.6}_{-1.7}$
CN1	+4.0 +2.0	327.4	$0.3^{+0.1}_{-0.1}$	$2.0^{+1.8}_{-0.7}$	<4.0*	<3.0*	$1.8^{+3.1}_{-0.6}$	>50	>4	$9.8^{+2.0}_{-2.0}$

Notes. Relative abundances wrt. H_2; (1) contaminated with methanol (see text); (*) 3σ limit.

the CN spectral maps, we identified one well-defined CN emission peak with weak counterpart in the other species. We refer to this position as CN1 and it corresponds to the ~326 km s^{-1} component toward E2 (see Figs. 7 and A.1). Figure A.3 shows the H(41)α PdBI spectral maps. This line probes the spatial distribution of the ionized gas that is closely related to the local UV field. GP4 is the most intense position in this radio recombination line. Secondary peaks are spatially coincident with GP1, CN1, and GP5, showing the presence of ionized gas at these positions. The absence of H(41)α emission toward SS2 and SS3 proves that there is a lower UV field in the sourthern part of the supershell. Therefore, our selected positions are representative of the different physical conditions, in particular the mean UV field, within this galaxy.

We have estimated the CN, N_2H^+, CS and C_3H_2 molecular column densities using the LVG code MADEX (Cernicharo 2012). Our observations do not allow a multitransitional study. Instead, we need to assume a uniform layer with constant physical conditions. On the basis of CO and its isotopologues, Weiss et al. (2001b) derived densities of $n(H_2) \sim 5 \times 10^4$ cm^{-3} and gas kinetic temperatures ranging from ≈50 K toward the E1 and W1 positions to ≈150 K toward E2 and W2. Later, Fuente et al. (2005) determined densities of 1×10^5 cm^{-3} from single-dish data of the CN $1 \rightarrow 0$ and $2 \rightarrow 1$ lines. Higher densities, $\sim 5 \times 10^5$ cm^{-3}, were estimated by Fuente et al. (2008) using the high-excitation $J = 3 \rightarrow 2$ and $4 \rightarrow 3$ lines of HCO^+. Bayet et al. (2009) proposed two components to fit the CS lines with densities of $\sim 10^5$ cm^{-3} and 6×10^5 cm^{-3} for the diffuse and dense components, respectively. These estimates proved that, as expected, different density components coexist within our beam. Since these are molecules with large dipole moments, we considered that the emission is dominated by dense gas with $n(H_2) > 1 \times 10^5$ cm^{-3}. To estimate the molecular column densities and the uncertainties in our calculations, we ran a grid of LVG models with $n(H_2)$ varying from 1×10^5–5×10^5 cm^{-3} and $T_k = 50, 150$ K and adopted the average value. The hyperfine structures of CN and N_2H^+ were not considered in our calculations because of the large line widths. The estimated column densities are shown in Table 2. The errors correspond to the lowest and highest values obtained in our grid, that is to say, these errors do not account for the observational errors, which are lower, but for the uncertainty in the physical conditions. In general, the uncertainties in the obtained column densities are within a factor of 2.

In our calculations we assumed that all the emission at 145.089 GHz comes from the c-C_3H_2 carrier, which is not true for some positions. Methanol was first detected by Martín et al. (2006) in M 82. Based on the kinematical and spatial distribution, they concluded that the emission mainly comes from the intense eastern and western knots at the outer part of the galaxy. Later, Aladro et al. (2011) performed a single-dish multitransitional study of CH_3OH anc c-C_3H_2 toward a position close to E1 and derived their column densities and rotational temperatures. We assumed these values to predict the expected CH_3OH and c-C_3H_2 line intensities and obtained that ~50% of the emission must belong to each carrier toward E1. According to these results, the c-C_3H_2 column density is overestimated by a factor of ~2 in E1. Taking into account the similarties between the molecular chemistry in E1 and W1, we consider that we very likely have a similar contamination, that is, ~50%, toward W1.

In Table 2, we also show the [CN]/[N_2H^+], [CS]/[N_2H^+] and [CN]/[CS] column density ratios toward the selected molecular knots. These values were estimated using the same procedure as for the column densities. We ran a grid of LVG models and adopted the average value of the fitted column density ratios. When molecules with similar excitation conditions are selected, this method minimizes the uncertainty due to the assumed physical conditions, because the uncertainties in the column density ratios is lower than those of the individual column densities (see Table 2).

Significant variations higher than the uncertainties are found in the [CN]/[N_2H^+] ratio across the galaxy. This ratio takes values ≈30 in GP1 and GP6 located in the outer $x1$ orbits and increases to ≈80 toward GP4. Values >50 are found toward GP5 and SS1, both close to W2. The lowest value, [CN]/[N_2H^+] ≈ 19, is found in the southern part of the supershell. In Fig. 9 we compare the obtained column density ratios with the integrated intensity maps of the N_2H^+ $1 \rightarrow 0$, H(41)α lines and SiO $2 \rightarrow 1$ lines. The good correlation between the values of the [CN]/[N_2H^+] ratio and the emission of the H(41)α line is remarkable and supports the interpretation that the variations of the [CN]/[N_2H^+] ratio are related to the variations of the local UV field. We did not find any correlation between the [CN]/[N_2H^+] ratio and the SiO emission.

The [CN]/[CS] ratio behaves similarly to that of [CN]/[N_2H^+]. It takes values ≈3.5 in GP1 and GP6 located in the outer $x1$ orbits and increases to >5 toward GP4, GP5, and SS1. In the case of CN1, we estimate a higher value of [CN]/[CS] ≈ 10. The correlation between the [CN]/[CS] ratio and the H(41)α emission is good.

In contrast to the [CN]/[N_2H^+] and [CN]/[CS] ratios, the [CS]/[N_2H^+] ratio remains quite constant across the galactic plane with values of about 12. There is no evidence of variation of this ratio with the local UV field. When comparing the galactic plane positions with those of the supershell, we realized that the ratio tends to be a factor of 2 lower in the southern part of the supershell, although always within the uncertainty of our calculations.

We used the $C^{18}O$ map from Weiss et al. (2001b) to determine the total molecular hydrogen column densities and absolute fractional abundances. The $C^{18}O$ column densities vary by only a factor of ~2 among the different knots, with the highest values in GP1 and GP6. Molecular abundances were derived from the N(X)/N($C^{18}O$) column density ratio assuming [$C^{18}O$]/[^{12}CO] = 0.005 and [^{12}CO] = 4×10^{-5}, which are the average values derived by Weiss et al. (2001b) on the basis of their multitransitional study of CO, ^{13}CO, and $C^{18}O$. Note that these values correspond to a $^{16}O/^{18}O$ ratio of 200, which is different from the Milky Way standard value of ~500–600. We assumed a constant $C^{18}O$ abundance throughout the galaxy, which is an approximation since the $C^{18}O$ abundance is dependent on the environment (UV flux, density, temperature). However, we are interested in the dense molecular gas ($n(H_2) > 1 \times 10^5$ cm^{-3}), and the $C^{18}O$ abundance is expected to remain roughly constant in this component. Following this procedure, we derived the molecular abundances shown in Table 2. The N_2H^+ abundance is $\sim 3 \times 10^{-11}$ for all the positions, corroborating that N_2H^+ is a good tracer of the dense molecular gas. An abundance of a few 10^{-10} is measured for CS. Small changes of lower than a factor of 2 are found in the abundances of this species; these are within the uncertainties of our calculations. Only the CN abundance presents significant variations within the galaxy; it is larger by a factor ~3 in GP4 than in the outer positions, GP1 and GP6, and in the southern supershell positions, SS2 and SS3.

4.2. Other species: H_2CO, HC_3N, and CH_3CN

To gain a more comprehensive view of the chemistry in M 82, we compared our new data with previous interferometric images.

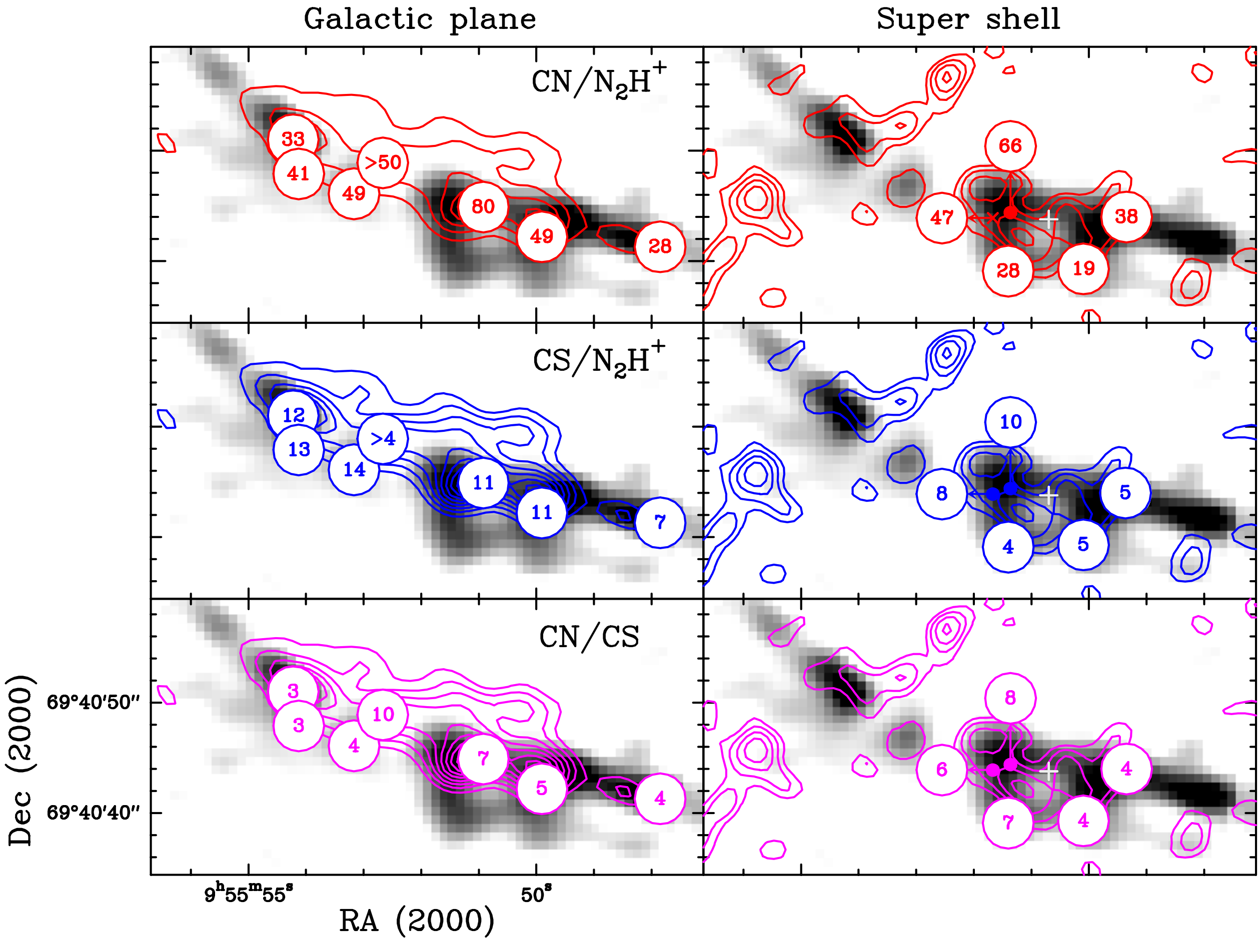

Fig. 9. [CN]/[N_2H^+], [CS]/[N_2H^+] and [CN]/[CS] abundance ratios for the positions listed in Table 2 in the galactic plane (*left*) and the supershell associated with SN 41.9+58 (*right*) superposed to the N_2H^+ 1 → 0 integrated intensity map (gray scale). For comparison, in the *left column* we plot the contours of the integrated intensity emission of the H (41) α line, and in the right, the integrated intensity emission of the SiO 2 → 1 line (García-Burillo et al. 2001). The white cross indicates the position of SN 41.9+58.

To this aim, we degraded the angular resolution of all our images to ≈5.9″ (≈111 pc), which is the lowest from the data set shown in Table 1, and used the total velocity-integrated line intensity in our calculations. The Gaussian fit parameters toward E1, E2, W2, and W1 are shown in Table A.1.

Column densities and column density ratios were calculated following the same procedure as in Sect. 4.1. In Table 3, we show the values obtained for E1, E2, W2, and W1. The [CS]/[$H^{13}CO^+$] and [$H^{13}CO^+$]/[$C^{18}O$] ratios are quite uniform across the galaxy. This suggests that CS, $H^{13}CO^+$, and $C^{18}O$ are good tracers of dense gas for a wide range of physical conditions. According to these results, E1 and W1 present the highest total molecular hydrogen column densities. This is consistent with the detection of complex molecules such as NH_3, HC_3N, CH_3CN, and CH_3OH toward them (Weiss et al. 2001a; Martín et al. 2006; Aladro et al. 2011). The small hydrocarbons c-C_3H_2 and C_4H are also good tracers of low- and high-UV PDRs (Fuente et al. 2003; Pety et al. 2005; Pilleri et al. 2013; Cuadrado et al. 2015). Taking into account that the abundance of c-C_3H_2 is very likely overestimated by a factor of ~2 in E1 and W1 (see Sect. 4), we conclude that the abundance of c-C_3H_2 could be enhanced by a factor of ~3 in the inner $x2$ orbits, in agreement with the trend observed in CN. Moreover, the derived H_2CO abundance is similar to that derived by Guzmán et al. (2013, 2014) in the Horsehead nebula and is consistent with the interpretation that the H_2CO emission comes from PDRs. Summarizing, the overall chemical behavior observed in M 82 is well interpreted as the consequence of the effect of UV radiation on the molecular chemistry. This produces an increase in the abundance of PDR tracers (CN, c-C_3H_2, H_2CO) toward E2 and W2, following the spatial distribution of HII regions. The detection of complex molecules shows that a fraction of the gas is protected from the UV radiation in the interior of large molecular clouds. The amount of gas in this shielded component is higher in the outer $x1$ bar orbits.

We recall that the position of W2 is related with supernova explosion SN 41.9+58 that launches ionized gas out of the galaxy plane. The detection of SiO by García-Burillo et al. (2001) proved the existence of shocks and their effect on the gas chemistry. H_2CO, CH_3OH, and CS are considered good tracers of shocks in galactic and extra-galactic environments (see e.g. Bachiller et al. 2001; García-Burillo et al. 2000; Usero et al. 2006). However, our data do not present any evidence of CS abundance enhancement caused by possible shocks. In fact, the [CS]/[N_2H^+] ratio is slightly lower in the supershell. This suggests that only a small fraction of the gas is affected by shocks, which is also consistent with the low average SiO abundance determined by García-Burillo et al. (2001), X(SiO) ~ 1×10^{-10}, when compared with the SiO abundances, ~10^{-8}–10^{-6}, found in the shocks associated with galactic star-forming regions (Martín-Pintado et al. 1992; Bachiller et al. 2001). We cannot analyze H_2CO and CH_3OH in detail because their lines are blended with other species.

Table 3. Fractional abudances and abundance ratios.

	E1	E2	W2	W1
$N(C^{18}O)$ ($\times 10^{16}$)	10^{+6}_{-4}	$4.1^{+2.5}_{-1.7}$	$4.8^{+2.7}_{-2.0}$	11^{+7}_{-4}
$X(CN)$ ($\times 10^{-9}$)	$1.4^{+0.5}_{-0.4}$	$3.2^{+1.0}_{-0.8}$	$4.0^{+1.4}_{-1.0}$	$1.2^{+3.8}_{-0.3}$
$X(N_2H^+)$ ($\times 10^{-11}$)	$2.4^{+0.6}_{-0.6}$	$3.1^{+0.6}_{-0.4}$	$4.4^{+0.8}_{-0.9}$	$2.0^{+0.4}_{-0.4}$
$X(CS)$ ($\times 10^{-10}$)	$5.2^{+2.4}_{-1.8}$	$7.2^{+3.6}_{-2.5}$	$7.8^{+3.6}_{-2.8}$	$4.3^{+2.0}_{-1.4}$
$X(H^{13}CO^+)$ ($\times 10^{-11}$)	$1.8^{+0.7}_{-0.7}$	$1.3^{+0.6}_{-0.6}$	$2.4^{+1.0}_{-0.8}$	$1.3^{+0.5}_{-0.5}$
$X(o\text{-}C_3H_2)$ ($\times 10^{-10}$)	$2.0^{+2.0}_{-1.2}$	$2.8^{+2.7}_{-1.8}$	$3.4^{+3.0}_{-2.2}$	$2.4^{+2.4}_{-1.6}$
$X(p\text{-}H_2CO)$ ($\times 10^{-11}$)	$7.4^{+5.8}_{-3.6}$	$>9.6^{+7.8*}_{-4.8}$	$>5.6^{+4.4*}_{-2.8}$	$4.6^{+3.8}_{-2.2}$
$X(HC_3N)$ ($\times 10^{-11}$)	$8.1^{+12}_{-6.5}$	$<13^{+19*}_{-11}$	$<31^{+46*}_{-25}$	$5.3^{+8.8}_{-4.2}$
$X(CH_3CN)$ ($\times 10^{-11}$)	$1.4^{+2.0}_{-0.6}$	$<1.0^{**}$	$<0.8^{**}$	$1.0^{+1.3}_{-0.4}$
$[CN]/[N_2H^+]$	56^{+13}_{-7}	101^{+29}_{-16}	92^{+18}_{-14}	58^{+14}_{-8}
$[CN]/[CS]$	$2.8^{+1.8}_{-1.0}$	$4.7^{+1.5}_{-1.7}$	$5.6^{+1.6}_{-2.1}$	$2.9^{+0.9}_{-0.9}$
$[CS]/[N_2H^+]$	20^{+6}_{-6}	17^{+13}_{-8}	23^{+9}_{-8}	21^{+7}_{-7}
$[H^{13}CO^+]/[N_2H^+]$	$0.7^{0.2}_{-0.2}$	$0.5^{+0.2}_{-0.2}$	$0.5^{+0.2}_{-0.2}$	$0.6^{+0.}_{-0.2}$

Notes. Beam (5.9″) average column densities resulting from LVG calculations in a grid with T_k = 50–150 K, and $n(H_2) = 1 \times 10^5$, 5×10^5. Errors correspond to the lowest and highest values in the grid. $^{(*)}$ Reasonable guess since HC_3N and H_2CO are blended at this position. $^{(**)}$ Upper limits have been derived assuming Δv = 50 km s^{-1}, T_k = 50 K and $n(H_2) = 5 \times 10^5$ cm^{-3}.

5. Chemical model

We used the Meudon PDR code 1.4.4 (Le Petit et al. 2006) to model the chemistry in M 82. In our calculations, we assumed that the ISM is composed of clouds bathed in an intense UV field. We simulated each cloud by a uniform plane-parallel layer illuminated from the two sides. This layer has constant density ($n = n(H) + 2 \times n(H_2) = 4 \times 10^5$ cm^{-3}), and the gas kinetic temperature was calculated by detailed heating and cooling balance. The adopted initial elemental abundances are the same as in Fuente et al. (2008). We ran a grid of models by varying the cloud size, UV field, and cosmic-ray ionization rate.

Our grid includes two values of the Draine field, 6×10^3 and 6×10^2. The first value was determined by Fuente et al. (2005, 2006, 2008) from the CO^+, HCO^+ and HOC^+ observations. The second value is considered to account for the possibility of regions with a lower UV field within the galaxy. To investigate the effect of the enhanced cosmic-ray flux on the chemistry, we repeated our model calculations with $\zeta = 5 \times 10^{-17}$ and 5×10^{-15} s^{-1}. The first value corresponds to the cosmic-ray ionization rate in the molecular clouds of our Galaxy (Indriolo et al. 2015). The second is the value estimated by Suchkov et al. (1993) to account for the physical conditions of the molecular gas in M 82. We are aware that X-rays are intense and could also play an important role in the chemistry (Fuente et al. 2008; Spaans & Meijerink 2007). Our code does not include the X-rays in the chemical calculations. We investigated the effect that X-rays could have on the chemistry by increasing the cosmic-ray ionization rate to 5×10^{-14} s^{-1}. To increase the cosmic-ray ionization rate reproduces the effect of X-rays on the molecular chemistry reasonably well, although it cannot account for the effect on the molecular gas heating. Finally, in our simple model, the cloud size is given by the total cloud visual extinction. We considered five values: 5 mag, 10 mag, 20 mag, 50 mag, and 100 mag.

In Fig. 10 and Table 4 we show the cloud average molecular abundances as a function of the different model parameters. The large dispersion in the values is not unexpected since all the parameters are varied by several orders of magnitude. The cloud average abundances of CN, N_2H^+, CS and HCO^+ increase with the cosmic-ray ionization rate. This increase is especially strong for N_2H^+. While the abundances of the other species increase by a factor of a few, the abundance of N_2H^+ increases by two orders of magnitude between $\zeta = 5 \times 10^{-17}$ and 5×10^{-14} s^{-1}. Surprisingly, the N_2H^+ abundance is quite constant in the studied knots. This suggests that the chemical changes we observe are not related with variation in the X-rays flux. We cannot discard, however, that variations in the UV field and cloud sizes could balance to keep the N_2H^+ abundance constant in spite of the variation of the X-rays flux (Strickland & Heckman 2007).

The cloud size has the strongest impact on the results of our model. N_2H^+ has a negligible abundance in clouds with $A_v <$ 10 mag and abundances varying between 10^{-10} and 10^{-9} for larger clouds. This corroborates our assumption that this species is an excellent tracer of the UV-protected molecular gas. The $[CN]/[N_2H^+]$ ratio is a good measure of the cloud size for one single cloud component. Fuente et al. (2008) proposed the existence of two cloud components towards E1: most of the mass, ~87%, is locked in small clouds of $A_v \sim 5$ mag, the remainder forms $A_v > 50$ mag clouds. In this case, the $[CN]/[N_2H^+]$ ratio would depend on both the fraction of each cloud component and the assumed size for the large clouds.

The cloud average CS abundance is quite constant for sizes between ~5 and ~20 mag but increases by almost one order of magnitude for larger sizes. The high values of the CS abundance in the 50 mag clouds are not reliable. The CS abundance is very dependent on the assumed elemental sulphur abundance. Our gas phase models do not consider the adsorption of molecules on the grain surfaces. Within our galaxy, the sulphur abundance measured in PDRs is a factor >4 lower than the solar value, suggesting that significant sulphur depletion occurs even in highly irradiated environments (see Goicoechea et al. 2006). Moreover, our model assumes a solar value for the sulphur elemental abundance, 1.8×10^{-5}, which could greatly differ from that in M 82 (Umeda et al. 2002; Origlia et al. 2004). Therefore, we do not consider that the values of the CS abundance predicted by our model are reliable.

The $[CN]/[N_2H^+]$ ratio is a sensitive tracer of the cloud size for sizes <50 mag. Other parameters such as the incident UV field and the cosmic-ray ionization rate could also affect the predicted $[CN]/[N_2H^+]$ ratio. As expected, the $[CN]/[N_2H^+]$ ratio increases for higher UV fluxes, especially for small clouds. In contrast, the $[CN]/[N_2H^+]$ ratio decreases with the cosmic-ray ionization rate because the N_2H^+ abundance increases. In the following, we discuss the cloud distribution in M 82 on the basis of the $[CN]/[N_2H^+]$ ratio. We use our a priori knowledge of the galaxy to constrain the chemical models. We discuss the results for one- and two-component models.

In Fig. 11, we plot the $[CN]/[N_2H^+]$ abundance ratio as a function of the cloud size for Draine fields of 6×10^3 (high-UV) and 6×10^2 (low-UV). We adopted the value derived by Suchkov et al. (1993) for the cosmic-ray ionization rate because it is the most likely. GP4 is the position with the highest value of the $[CN]/[N_2H^+]$ ratio and also the emission peak of the H(41)α line. It is reasonable to assume that high-UV models, the red lines in Fig. 11, are more adequate to account for the molecular abundances at this position. One single-cloud component with sizes of ~22 mag could explain the observed $[CN]/[N_2H^+]$ ratio of ~80. Lower $[CN]/[N_2H^+]$ ratios, ~30, are measured toward the positions GP1 and GP6. Although less intense, these knots are also associated with peaks in the H(41)α line emission, which

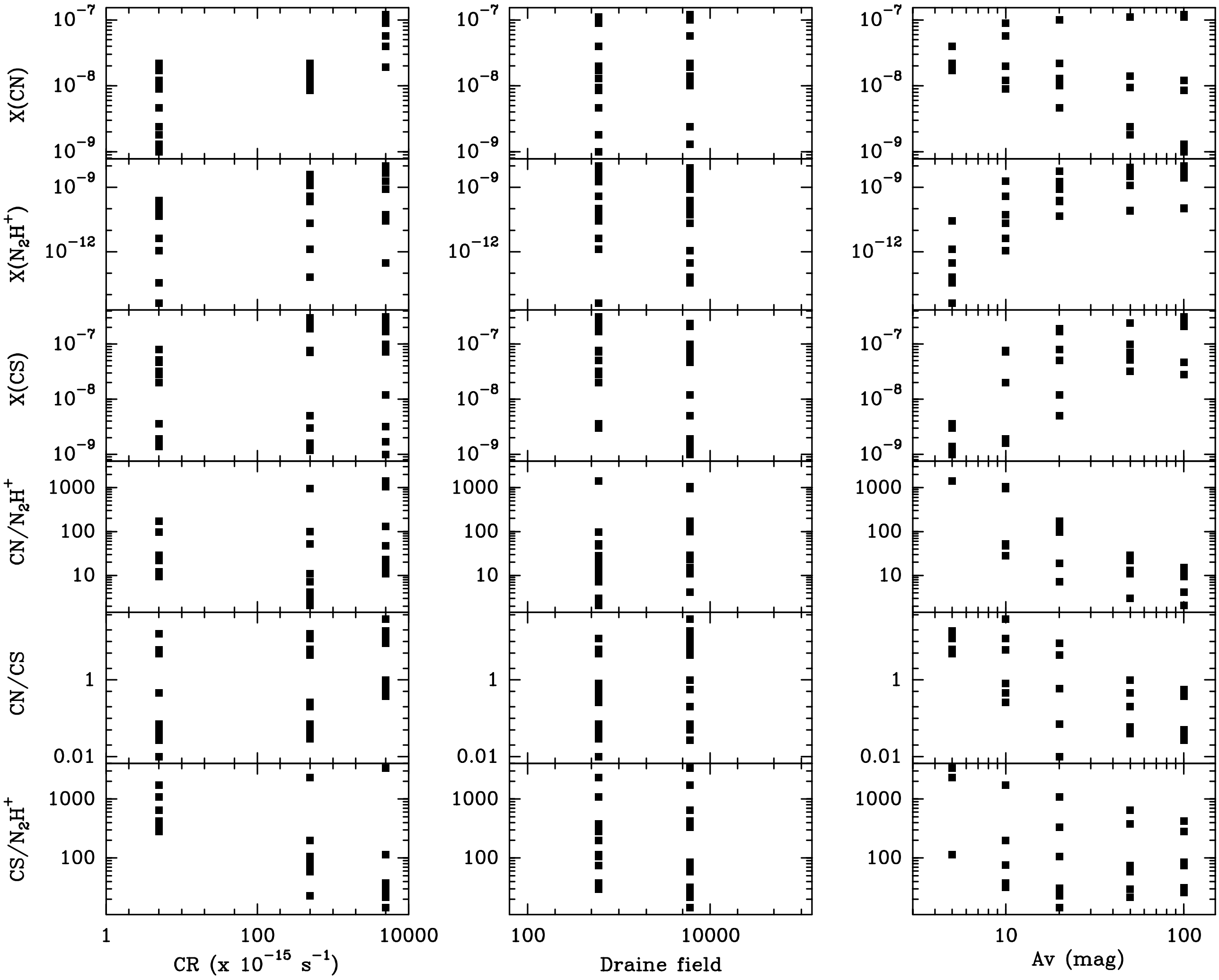

Fig. 10. Model predictions as a function of the cosmic-ray ionization rate, Draine field, and cloud size. Model parameters and results are shown in Table 4.

proves that there are energetic UV photons capable of ionizing the atomic hydrogen (see Fig. A.3). Assuming the high-UV case, the lower [CN]/[N$_2$H$^+$] ratio can be explained by the existence of a population of larger clouds, ~30 mag (see Fig. 11). The existence of larger clouds is also consistent with the lower kinetic temperatures and higher densities measured by Weiss et al. (2001b) and the detection of complex molecules at these positions. Low values of the [CN]/[N$_2$H$^+$] ratio, ~20−30, are also observed toward the SS2 and SS3 points placed in the molecular supershell. Since there is a lack of H(41) α emission toward these positions, we used the low-UV field models to interpret the [CN]/[N$_2$H$^+$] ratio and obtained that the molecular emission could come from translucent clouds of ~14 mag.

We conclude from our one-component model that the variation of the average cloud size is compatible with the results of Fuente et al. (2008), who interpreted the abundances in E1 in a two-component scenario. We can use a two-component model to explain our observations. In this case, the CN emission would come from the small (with A_v ~ 5 mag) and large (with A_v ~ 50 mag) molecular clouds, while the N$_2$H$^+$ emission would come only from large molecular clouds. Fuente et al. (2008) estimated that only ~13% of the molecular gas is forming large molecular clouds in E1. Assuming the same fraction at all positions, the [CN]/[N$_2$H$^+$] ratio in the large cloud component would be about 0.13 times the observed one, that is, ~10 in GP4, ~4 in GP1 and ~3 in SS3, meaning that we would have clouds of >50 mag in the three positions, with the largest ones, ~100 mag, toward GP1. In summary, both the one- and two-components models allow the conclusion that the highest concentration of UV-protected molecular gas is found toward the $x1$ orbits. The detection of complex molecules is better understood in terms of two populations of clouds with a small fraction of the gas, ~13%, locked in giant molecular clouds where the gas is UV protected and can form large molecules.

Of course, the two models are very simple and have to be understood as a guide for interpreting the molecular chemistry in this starburst galaxy. As commented above, our model neglects the surface chemistry and X-ray effets that could be important for some species (see discussion above). Moreover, our gas phase model assumes steady-state chemistry. The characteristic time for PDR chemistry is $\tau \sim 1/(\kappa_d\, G_0)$, where κ_d is the photodissociation rate in s^{-1} and G_0 is the incident UV field in Habing units. The value of κ_d depends on the extinction from the illuminating source as $\kappa_d \sim \kappa_0 \times \exp(-b\, A_v)$. Assuming a typical value of $\kappa_0 = 10^{-9}$ s^{-1}, $b = 1.8$ and the incident mean UV interstellar field in M 82, $G_0 = 10^4$ Habing fields, the characteristic time is >10 Myr for $A_v > 2.5$ mag. This means that if the last starburst episode took place about ~5−10 Myr ago, the chemistry might be out of equilibrium in the cloud interior. Our steady-state scenario is therefore only adequate for the cloud

Table 4. Chemical models.

Model	CR ($\times 10^{-17}$)	Cloud size (mag)	Draine field	X(CN)	X(N_2H^+)	X(CS)	[CN]/[N_2H^+]	[CN]/[CS]	[CS]/[N_2H^+]
High-UV									
1	5000	100	6e3	1.2e-7	8.0e-9	2.1e-7	15	0.56	27
2	500	100	6e3	1.2e-8	2.8e-9	2.4e-7	4.2	0.05	85
3	5	100	6e3	1.3e-9	1.1e-10	4.7e-8	12	0.03	439
4	5000	50	6e3	1.1e-7	4.6e-9	1.0e-7	23	1.0	22
5	500	50	6e3	1.4e-8	1.2e-9	7.0e-8	11	0.2	58
6	5	50	6e3	2.4e-9	8.1e-11	5.2e-8	29	0.05	641
7	5000	20	6e3	1.0e-7	8.3e-10	1.2e-8	130	9.0	14
8	500	20	6e3	2.2e-8	2.2e-10	5.0e-9	100	4.4	22
9	5	20	6e3	1.0e-8	2.4e-10	8.0e-8	2173	0.07	333
10	5000	10	6e3	5.7e-8	5.3e-11	1.7e-9	1055	38	32
11	500	10	6e3	2.0e-8	2.1e-11	1.6e-9	952	12	76
12	5	10	6e3	1.2e-8	1.1e-12	1.9e-9	1.0e4	6	1727
13	5000	5	6e3	1.9e-8	3.0e-13	1.0e-9	6.4e4	19	3333
14	500	5	6e3	2.0e-8	6.4e-14	1.2e-9	3.1e5	16	18750
15	5	5	6e3	2.2e-8	3.6e-14	1.4e-9	6.1e5	16	38889
Low-UV									
16	5000	100	6e2	1.1e-7	1.0e-8	3.1e-7	11	0.38	30
17	500	100	6e2	8.6e-9	4.0e-9	3.0e-7	2.1	0.03	74
18	5	100	6e2	9.9e-10	1.0e-10	2.8e-8	9.4	0.03	270
19	5000	50	6e2	1.1e-7	8.2e-9	2.4e-7	13	0.45	29
20	500	50	6e2	9.4e-9	3.2e-9	2.4e-7	3	0.04	75
21	5	50	6e2	1.8e-9	8.4e-11	3.2e-8	122	0.06	380
22	5000	20	6e2	1.0e-7	5.5e-9	1.7e-7	19	0.59	31
23	500	20	6e2	1.3e-8	1.8e-9	1.9e-7	7	0.07	105
24	5	20	6e2	4.6e-9	4.6e-11	5.0e-8	98	0.01	1086
25	5000	10	6e2	8.9e-8	1.9e-9	7.2e-8	47	0.81	37
26	500	10	6e2	2.0e-8	3.8e-10	7.6e-8	52	0.26	200
27	5	10	6e2	9.0e-9	4.3e-12	2.0e-8	28	0.45	4651
28	5000	5	6e2	4.0e-8	2.8e-11	3.2e-9	1428	12	114
29	500	5	6e2	1.8e-8	1.3e-12	3.0e-9	1.4e4	6	2307
30	5	5	6e2	1.7e-8	4.0e-15	3.6e-9	4.3e6	5	9E5

Notes. Notation: 6e3 = 6×10^3.

surfaces and small clouds. The shortcoming of time-dependent models is that they depend on the initial conditions and require of a more sophisticated analysis, which is beyond the scope of this paper. Subsequent improvement of our current interpretation would require coupling the star formation history in this galaxy with a time-dependent PDR code that includes surface chemistry (Bayet et al. 2009; Viti et al. 2014; Bisbas et al. 2012).

For all species, the estimated fractional abundances in M 82 are lower than those predicted by our gas-phase model. Absolute fractional abundances are difficult to compare with models because of the large uncertainty in the total molecular gas column density. Weiss et al. (2001b) derived the total molecular gas column densities in M 82 using different methods: LVG calculations, a local thermodynamic equilibrium (LTE) solution, and the standard X_{CO} conversion factor, and their results agree within a factor ~3−4. In this paper, we derived the molecular column density toward the different points using the $C^{18}O$ data and assuming the CO abundance derived by Weiss et al. (2001b), X(CO) = 5×10^{-5}. We would like to note that this value is already lower than the value predicted by our model for large clouds in which essentially all the carbon is in CO with an abundance of $\sim 1.3 \times 10^{-4}$. Therefore our fractional abundances are accurate to within a factor of 4–10 and are consequently roughly consistent with model predictions.

6. PDR and shock chemistry in M 82

M 82 has been subject to successive starburst episodes in the past ~200 Gyr. The most recent (~5 Myr) took place throughout the central regions of M 82 and was particularly intense in the $x2$ orbits and along the stellar bar. The negative feedback effects from this starburst activity determine the existence and duration of future starburst episodes. We have carried out a chemical study of the molecular gas at scales of ~100 pc to investigate the feedback effects and the future star formation activity of the galaxy.

Our main result is that the chemistry of the molecular gas is determined by the intense UV radiation produced by the massive stars. There is a systematic variation of the studied molecular

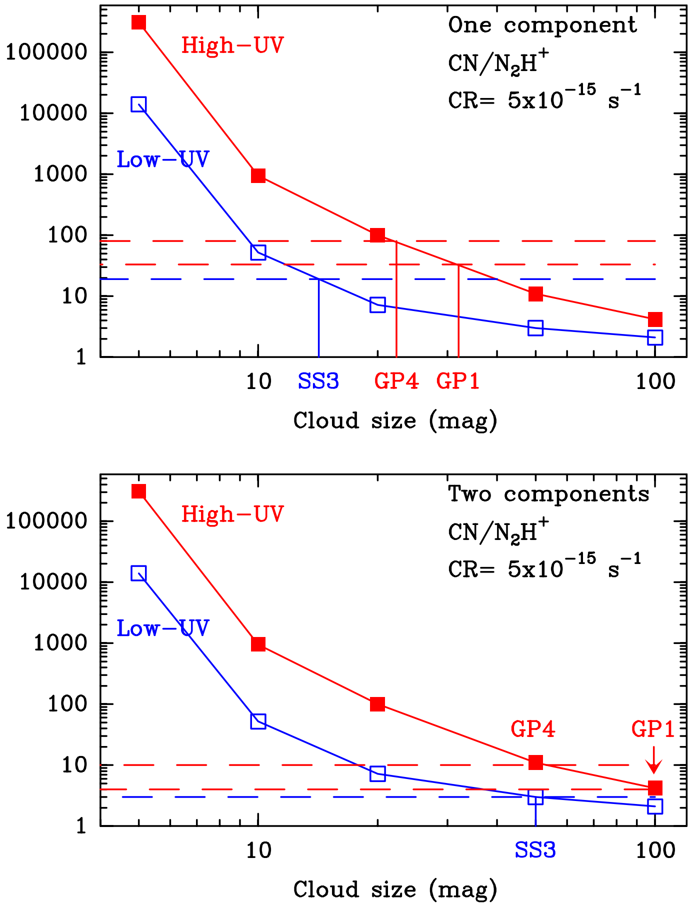

Fig. 11. [CN]/[N_2H^+] abundance ratio as a function of the cloud size for models with CR = 5×10^{-15} s^{-1} and Draine fields of 6×10^3 (red line) and $\times10^3$ (blue line). *Top*: cloud sizes in the one-component model. *Bottom*: sizes of the large cloud component in the two-component model (see text). The values and errors for GP1, GP4, and SS3 are indicated.

abundance ratios with the intensity of the H(41)α emission that corroborates that the whole nucleus (~650 pc), down to scales of ~100 pc, behaves like a giant PDR. Within this PDR, we have chemical variations due to changes in the local UV field and in the structure of the molecular clouds. There are three clearly differentiated regions:

- The inner $x2$ bar orbits, which are associated with the most recent starburst and where the PDR tracers present their peak abundances. The detection of N_2H^+ in these regions proves that molecular clouds of >20 mag are present and that therefore the molecular gas reservoir to form new stars is not exhausted.
- The outer $x1$ bar orbits where most the UV-protected molecular gas is located. The detection of H(41)α shows that massive stars have already been formed in these clouds.
- The molecular supershell associated with the supernova remnant SN 41.9+58. There are no signs of massive star formation activity in the southern part of this supershell, although there are intense N_2H^+ knots that could be sites for future star formation.

The detection of a ~500 pc molecular gas chimney and a supershell in SiO indicates the occurrence of large-scale shocks in the disk-halo interface (García-Burillo et al. 2001). We recall that the supershell is related with the supernova explosion SN 41.9+58, which launches ionized gas out of the galaxy plane. However, our data do not present any evidence of possible shock chemistry. This suggests that only a small fraction of the dense molecular gas is affected by shocks, which is also consistent with the low SiO abundance determined by García-Burillo et al. (2001), X(SiO) ~ 1×10^{-10}, when compared with the SiO abundances, ~10^{-8}–10^{-6}, found in the shocks associated with galactic star-forming regions (Martín-Pintado et al. 1992; Bachiller et al. 2001). Higher spatial resolution observations are required to detect the layer of molecular gas around the supershell, whose chemistry is dominated by shocks. This is also consistent with the moderate fraction of dense molecular gas (~2%) that Salas et al. (2014) detected in the halo, in contrast with ~25% found by Walter et al. (2002) on the basis of CO observations. Most of the expelled gas presents moderate densities and is not detected in dense molecular tracers.

In summary, we presented a comprehensive chemical study of the molecular gas in the starburst galaxy M 82 using high spatial resolution (60–100 pc) interferometric images. Our chemical study showed that the feedback effects are strong in this evolved starburst. In fact, the whole nucleus presents a PDR-like chemistry, which suggests that UV radiation is driven by the subsequent evolution of the ISM. However, the detection of N_2H^+ proves the existence of dense molecular gas enclosed in clouds of A_v > 20 mag that could form new stars. The main reservoir of the dense molecular gas is located in the outer $x1$ orbits that might be the preferred site for a new generation of stars if the inside-outside scenario is assumed.

Acknowledgements. A.F. thanks the Spanish MINECO for funding support from grants CSD2009-00038 and AYA2012-32032. S.G.B. acknowledges support from Spanish grants CSD2009-00038, AYA2010-15169, AYA2012-32295, AYA2013-42227-P and from the Junta de Andalucia through TIC-114 and the Excellence Project P08-TIC-03531. P.P. acknowledges financial support from the Centre National d'Études Spatiales (CNES).

References

Achtermann, J. M., & Lacy, J. H. 1995, ApJ, 439, 163
Aladro, R., Martín, S., Martín-Pintado, J., et al. 2011, A&A, 535, A84
Bachiller, R., Fuente, A., Bujarrabal, V., et al. 1997, A&A, 319, 235
Bachiller, R., Pérez Gutiérrez, M., Kumar, M. S. N., & Tafalla, M. 2001, A&A, 372, 899
Bayet, E., Viti, S., Williams, D. A., Rawlings, J. M. C., & Bell, T. 2009, ApJ, 696, 1466
Bisbas, T. G., Bell, T. A., Viti, S., Yates, J., & Barlow, M. J. 2012, MNRAS, 427, 2100
Boger, G. I., & Sternberg, A. 2005, ApJ, 632, 302
Bregman, J. N., Schulman, E., & Tomisaka, K. 1995, ApJ, 439, 155
Cernicharo, J. 2012, EAS Pub. Ser., 58, 251
Cuadrado, S., Goicoechea, J. R., Pilleri, P., et al. 2015, A&A, 575, A82
Förster Schreiber, N. M., Genzel, R., Lutz, D., & Sternberg, A. 2003, ApJ, 599, 193
Fuente, A., Martín-Pintado, J., Cernicharo, J., & Bachiller, R. 1993, A&A, 276, 473
Fuente, A., Martin-Pintado, J., & Gaume, R. 1995, ApJ, 442, L33
Fuente, A., Rodrıguez-Franco, A., Garcıa-Burillo, S., Martın-Pintado, J., & Black, J. H. 2003, A&A, 406, 899
Fuente, A., García-Burillo, S., Gerin, M., et al. 2005, ESA SP, 577, 281
Fuente, A., García-Burillo, S., Gerin, M., et al. 2006, ApJ, 641, L105
Fuente, A., García-Burillo, S., Usero, A., et al. 2008, A&A, 492, 675
García-Burillo, S., Martín-Pintado, J., Fuente, A., & Neri, R. 2000, A&A, 355, 499
García-Burillo, S., Martín-Pintado, J., Fuente, A., & Neri, R. 2001, ApJ, 563, L27
García-Burillo, S., Martín-Pintado, J., Fuente, A., Usero, A., & Neri, R. 2002, ApJ, 575, L55
Goicoechea, J. R., Pety, J., Gerin, M., et al. 2006, A&A, 456, 565
Greve, A. 2011, A&A, 529, A51
Greve, A., Wills, K. A., Neininger, N., & Pedlar, A. 2002, A&A, 383, 56
Guzmán, V. V., Goicoechea, J. R., Pety, J., et al. 2013, A&A, 560, A73
Guzmán, V. V., Pety, J., Gratier, P., et al. 2014, Faraday Discuss., 168, 103

Indriolo, N., Neufeld, D. A., Gerin, M., et al. 2015, ApJ, 800, 40
Joy, M., Lester, D. F., & Harvey, P. M. 1987, ApJ, 319, 314
Kronberg, P. P., Biermann, P., & Schwab, F. R. 1981, ApJ, 246, 751
Le Petit, F., Nehmé, C., Le Bourlot, J., & Roueff, E. 2006, ApJS, 164, 506
Lester, D. F., Gaffney, N., Carr, J. S., & Joy, M. 1990, ApJ, 352, 544
Liszt, H., & Lucas, R. 2001, A&A, 370, 576
Mao, R. Q., Henkel, C., Schulz, A., et al. 2000, A&A, 358, 433
Martín, S., Martín-Pintado, J., & Mauersberger, R. 2006, A&A, 450, L13
Martín-Pintado, J., Bachiller, R., & Fuente, A. 1992, A&A, 254, 315
Murray, N. 2011, ApJ, 729, 133
Neininger, N., Guelin, M., Klein, U., Garcia-Burillo, S., & Wielebinski, R. 1998, A&A, 339, 737
Origlia, L., Ranalli, P., Comastri, A., & Maiolino, R. 2004, ApJ, 606, 862
Pety, J., Teyssier, D., Fossé, D., et al. 2005, A&A, 435, 885
Pilleri, P., Treviño-Morales, S., Fuente, A., et al. 2013, A&A, 554, A87
Salas, P., Galaz, G., Salter, D., et al. 2014, ApJ, 797, 134
Shen, J., & Lo, K. Y. 1995, ApJ, 445, L99
Shopbell, P. L., & Bland-Hawthorn, J. 1998, ApJ, 493, 129
Spaans, M., & Meijerink, R. 2007, ApJ, 664, L23
Strickland, D. K., & Heckman, T. M. 2007, ApJ, 658, 258
Suchkov, A., Allen, R. J., & Heckman, T. M. 1993, ApJ, 413, 542
Umeda, H., Nomoto, K., Tsuru, T. G., & Matsumoto, H. 2002, ApJ, 578, 855
Usero, A., García-Burillo, S., Martín-Pintado, J., Fuente, A., & Neri, R. 2006, A&A, 448, 457
Viti, S., García-Burillo, S., Fuente, A., et al. 2014, A&A, 570, A28
Walter, F., Weiss, A., & Scoville, N. 2002, ApJ, 580, L21
Weiß, A., Walter, F., Neininger, N., & Klein, U. 1999, A&A, 345, L23
Weiß, A., Neininger, N., Henkel, C., Stutzki, J., & Klein, U. 2001a, ApJ, 554, L143
Weiß, A., Neininger, N., Hüttemeister, S., & Klein, U. 2001b, A&A, 365, 571
Wills, K. A., Redman, M. P., Muxlow, T. W. B., & Pedlar, A. 1999, MNRAS, 309, 395
Wills, K. A., Das, M., Pedlar, A., Muxlow, T. W. B., & Robinson, T. G. 2000, MNRAS, 316, 33

Pages 16 to 19 are available in the electronic edition of the journal at http://www.aanda.org

Appendix A: Tables and figures

Table A.1. Gaussian parameters of the observed spectra.

Line		Freq.(GHz)	I(K km s^{-1})	$v_{\rm lsr}$(km s^{-1})	Δv(km s^{-1})	$T_{\rm MB}$(K)
			E1 (+14″, +5″)			
CN	$1 \rightarrow 0$	113.491	64.15 (0.56)	316.26 (0.33)	75.73 (0.77)	0.79
$H^{13}CO^+$	$1 \rightarrow 0$	86.754	4.52 (0.67)	324.66 (5.02)	69.39 (12.4)	0.06
H	41α	92.034	5.42 (0.19)	320.48 (1.21)	70.79 (2.89)	0.07
CH_3CN	$5_k \rightarrow 4_k{}^*$	91.987	2.43 (0.20)	328.58 (3.13)	74.26 (6.62)	0.03
N_2H^+	$1 \rightarrow 0$	93.173	6.98 (0.17)	321.42 (0.73)	60.23 (1.57)	0.11
$C^{18}O$	$1 \rightarrow 0$	109.782	22.74 (0.62)	324.40 (0.93)	69.58 (2.18)	0.31
C_3H_2	$3 \rightarrow 2$	145.089	9.90 (0.24)	315.23 (0.75)	63.77 (1.69)	0.14
H_2CO	$2_{0,2} \rightarrow 1_{0,1}$	145.603	8.45 (0.20)	321.30 (0.67)	56.90 (1.58)	0.14
HC_3N	$16 \rightarrow 15$	145.561	4.35 (0.17)	330.32 (0.90)	43.12 (1.96)	0.09
CS	$3 \rightarrow 2$	145.760	31.84 (0.37)	322.56 (0.32)	55.63 (0.71)	0.54
			E2 (+5″, +2″)			
Line		Freq.(GHz)	I(K km s^{-1})	$v_{\rm lsr}$(km s^{-1})	Δv(km s^{-1})	$T_{\rm MB}$(K)
CN	$1 \rightarrow 0$	113.491	56.09 (0.53)	249.23 (0.35)	79.56 (0.92)	0.66
			4.83 (0.30)	330.76 (0.78)	26.26 (1.70)	0.17
$H^{13}CO^+$	$1 \rightarrow 0$	86.754	2.19 (0.30)	258.66 (4.28)	57.14 (7.48)	0.03
H	41α	92.034	7.25 (0.24)	278.04 (1.89)	121.01 (5.46)	0.06
CH_3CN	$5_k \rightarrow 4_k{}^*$	91.987	1.35 (0.20)	284.18 (5.79)	85.36 (13.7)	0.01
N_2H^+	$1 \rightarrow 0$	93.173	3.74 (0.15)	255.80 (1.08)	58.24 (2.89)	0.06
$C^{18}O$	$1 \rightarrow 0$	109.782	9.22 (0.65)	259.28 (1.78)	53.14 (4.66)	0.16
C_3H_2	$3 \rightarrow 2$	145.089	4.95 (0.17)	245.88 (0.88)	53.58 (2.13)	0.09
			0.57 (0.12)	311.92 (2.90)	26.65 (5.71)	0.02
H_2CO	$2_{0,2} \rightarrow 1_{0,1}$	145.603	4.34 (0.16)	256.14 (0.77)	45.57 (1.98)	0.09
$HC_3N+H_2CO^a$		145.561	2.85 (0.17)	253.33 (1.48)	53.47 (3.90)	0.05
CS	$3 \rightarrow 2$	146.969	16.83 (0.15)	258.63 (0.20)	46.79 (0.53)	0.34
			1.43 (0.11)	329.47 (0.94)	25.13 (2.28)	0.05
			W2 (–5″, –2″)			
Line		Freq.(GHz)	I(K km s^{-1})	$v_{\rm lsr}$(km s^{-1})	Δv(km s^{-1})	$T_{\rm MB}$(K)
CN	$1 \rightarrow 0$	113.491	10.65 (0.82)	95.78 (0.37)	25.788 (1.18)	0.39
			56.67 (0.59)	99.31 (0.62)	92.166 (2.18)	0.58
			20.75 (0.54)	156.73 (1.09)	68.352 (1.92)	0.28
$H^{13}CO^+$	$1 \rightarrow 0$	86.754	2.86 (0.50)	115.70 (10.6)	111.91 (18.2)	0.02
H	41α	92.034	10.75 (0.29)	103.65 (0.59)	81.50 (1.71)	0.12
			8.87 (0.39)	172.86 (7.51)	352.24 (18.08)	0.02
CH_3CN	$5_k \rightarrow 4_k{}^*$	91.987				<0.015
N_2H^+	$1 \rightarrow 0$	93.173	3.85 (0.13)	93.13 (6.28)	48.56 (6.28)	0.07
			1.47 (0.13)	145.67 (6.28)	35.74 (6.28)	0.04
			0.91 (0.13)	183.60 (6.28)	30.43 (6.28)	0.03
$C^{18}O$	$1 \rightarrow 0$	109.782	10.45 (0.60)	130.29 (3.30)	111.32 (7.20)	0.09
C_3H_2	$3 \rightarrow 2$	145.089	4.72 (0.20)	89.20 (1.04)	55.84 (2.74)	0.08
			2.98 (0.21)	162.01 (0.31)	64.91 (4.64)	0.04
H_2CO^*	$2_{0,2} \rightarrow 1_{0,1}$	145.603	2.96 (0.25)	95.22 (0.90)	37.15 (2.58)	0.07
$HC_3N+H_2CO^b$		145.561	8.20 (0.70)	93.10 (3.30)	93.54 (10.92)	0.08
CS	$3 \rightarrow 2$	146.969	10.96 (2.52)	96.54 (3.24)	37.31 (4.49)	0.27
			7.77 (3.55)	136.99 (4.27)	42.03 (16.7)	0.17
			4.22 (1.47)	182.91 (4.92)	34.698.89)	0.11
			W1 (–14″, –5″)			
Line		Freq.(GHz)	I(K km s^{-1})	$v_{\rm lsr}$(km s^{-1})	Δv(km s^{-1})	$T_{\rm MB}$(K)
CN	$1 \rightarrow 0$	113.491	62.38 (0.58)	103.05 (0.36)	80.399 (0.87)	0.73
$H^{13}CO^+$	$1 \rightarrow 0$	86.754	3.90 (0.57)	104.39 (5.51)	76.888 (13.54)	0.05
H	41α	92.034	4.76 (0.18)	98.51 (1.52)	80.41 (3.65)	0.06
CH_3CN	$5_k \rightarrow 4_k{}^*$	91.987	1.78 (0.17)	127.93 (3.60)	71.73 (7.26)	0.02
N_2H^+	$1 \rightarrow 0$	93.173	6.61 (0.16)	113.57 (0.74)	62.23 (1.81)	0.10
$C^{18}O$	$1 \rightarrow 0$	109.782	24.90 (0.51)	118.46 (0.65)	63.32 (1.45)	0.37
C_3H_2	$3 \rightarrow 2$	145.089	13.00 (0.72)	103.29 (1.55)	57.80 (3.92)	0.21
H_2CO	$2_{0,2} \rightarrow 1_{0,1}$	145.603	6.12 (0.51)	110.67 (1.18)	47.71 (2.57)	0.12
HC_3N	$16 \rightarrow 15$	145.561	3.66 (1.52)	100.41 (18.4)	93.16 (43.1)	0.04
CS	$3 \rightarrow 2$	145.760	29.52 (0.26)	116.01 (0.24)	54.22 (0.55)	0.51

Notes. The PdBI images have been convolved to the same angular resolution (5.9″ × 5.9″). [*] The $k = 0, 1, 2$ and 3 components are blended. The velocity of the Gaussian fit is calculated relative to the frequency of the $k = 0$ component, ν = 91 987 MHz. [a] The ~326 km s^{-1} component of H_2CO overlaps with the ~270 km s^{-1} component of HC_3N. [b] A possible ~180 km s^{-1} component of H_2CO would overlap with the ~93 km s^{-1} component of HC_3N.

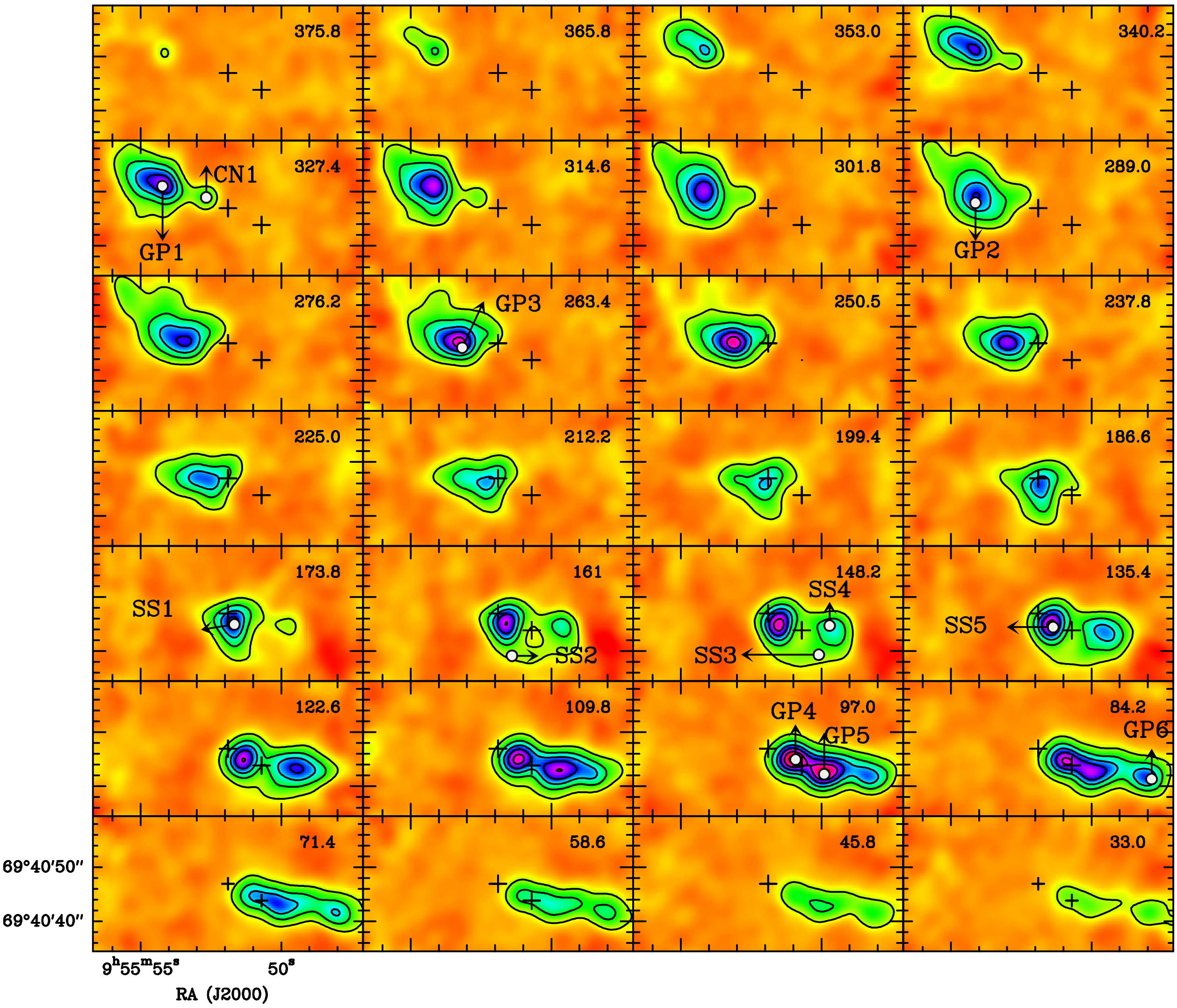

Fig. A.1. Spectral maps of the CN 1 → 0 line convolved to an angular resolution of 3.8″. To increase the signal-to-noise ratio, the velocity resolution has been degraded to 12.8 km s^{-1}. The number in the upper right corner indicates the central channel velocity. Contour levels are 0.17 ($5\times\sigma$) to 1.955 in steps of 0.255 K. Crosses indicate the dynamical center of the galaxy and the position of SN 41.9+58.

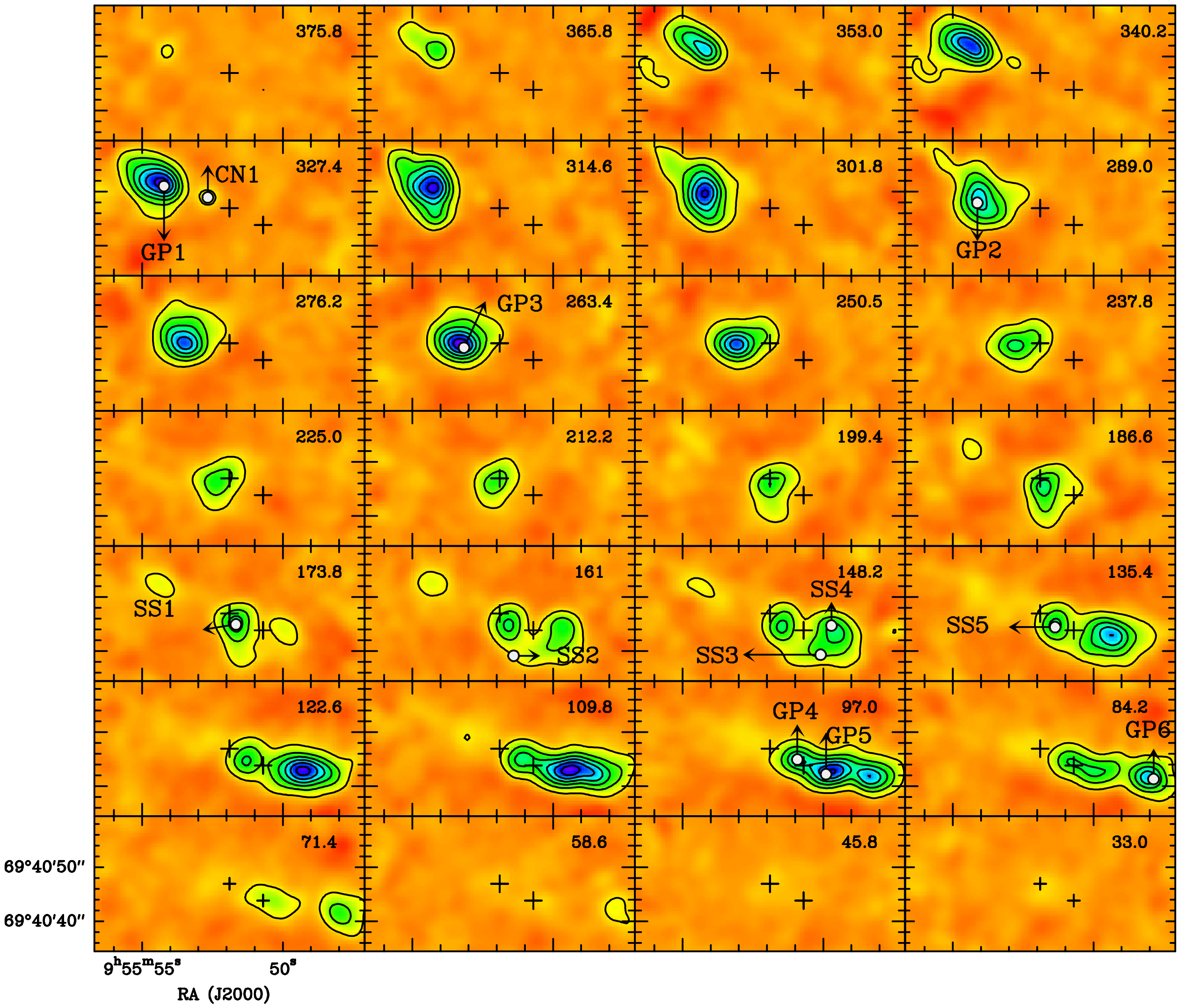

Fig. A.2. Same as Fig. A.1 for the CS 3 → 2 line. Contour levels are 0.065 (3 × σ) to 1.495 in steps of 0.13 K. The eastern knot at velocities ~144−192 km s^{-1} is due to the emission of the H(35)α line.

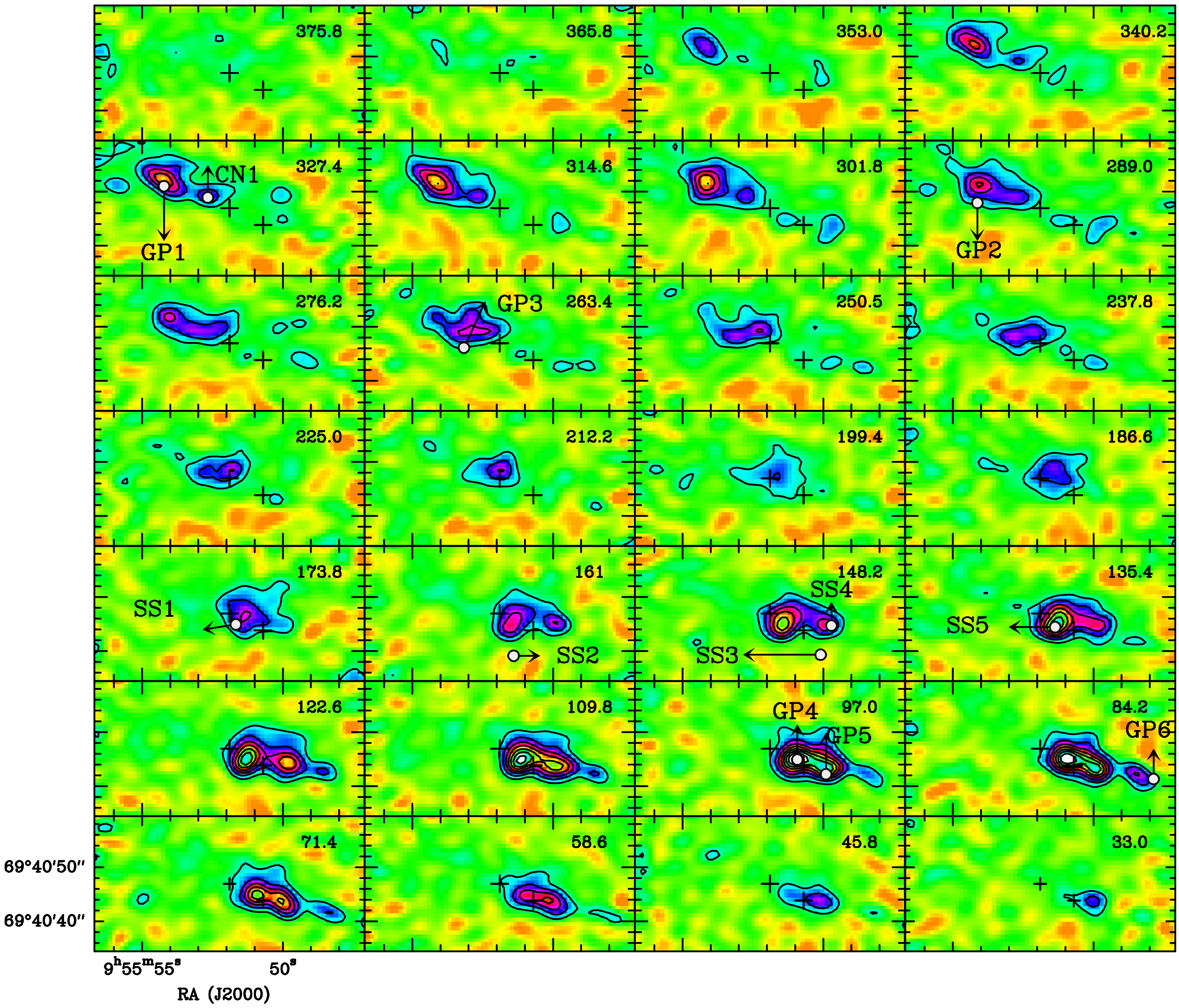

Fig. A.3. Same as Fig. A.1 for the H(41)α line. First contour and steps are 0.028 K ($\sim 3 \times \sigma$).